The Astrophysical Journal, 975:85 (25pp), 2024 November 1 https://doi.org/10.3847/1538-4357/ad66cc

To High Redshift and Low Mass: Exploring the Emergence of Quenched Galaxies and Their Environments at $3 < z < 6$ in the Ultra-deep JADES MIRI F770W Parallel

Stacey Alberts[1], Christina C. Williams[1,2], Jakob M. Helton[1], Katherine A. Suess[3,17], Zhiyuan Ji[1], Irene Shivaei[4], Jianwei Lyu[1], George Rieke[5], William M. Baker[6,7], Nina Bonaventura[1], Andrew J. Bunker[8], Stefano Carniani[9], Stephane Charlot[10], Emma Curtis-Lake[11], Francesco D'Eugenio[6,7], Daniel J. Eisenstein[12], Anna de Graaff[13], Kevin N. Hainline[1], Ryan Hausen[14], Benjamin D. Johnson[12], Roberto Maiolino[6,7], Eleonora Parlanti[9], Marcia J. Rieke[1], Brant E. Robertson[15], Yang Sun[1], Sandro Tacchella[6,7], Christopher N. A. Willmer[1], and Chris J. Willott[16]

[1] Steward Observatory, University of Arizona, 933 North Cherry Avenue, Tucson, AZ 85721, USA; salberts@arizona.edu
[2] NSF's National Optical-Infrared Astronomy Research Laboratory, 950 North Cherry Avenue, Tucson, AZ 85719, USA
[3] Kavli Institute for Particle Astrophysics and Cosmology and Department of Physics, Stanford University, Stanford, CA 94305, USA
[4] Centro de Astrobiología (CAB), CSIC-INTA, Ctra. de Ajalvir km 4, Torrejón de Ardoz, E-28850, Madrid, Spain
[5] Steward Observatory and Dept of Planetary Sciences, University of Arizona, 933 North Cherry Avenue, Tucson, AZ 85721, USA
[6] Kavli Institute for Cosmology, University of Cambridge, Madingley Road, Cambridge, CB3 0HA, UK
[7] Cavendish Laboratory, University of Cambridge, 19 JJ Thomson Avenue, Cambridge, CB3 0HE, UK
[8] Department of Physics, University of Oxford, Denys Wilkinson Building, Keble Road, Oxford OX13RH, UK
[9] Scuola Normale Superiore, Piazza dei Cavalieri 7, I-56126 Pisa, Italy
[10] Sorbonne Université, CNRS, UMR 7095, Institut d'Astrophysique de Paris, 98 bis bd Arago, 75014 Paris, France
[11] Centre for Astrophysics Research, Department of Physics, Astronomy and Mathematics, University of Hertfordshire, Hatfield, AL10 9AB, UK
[12] Center for Astrophysics | Harvard & Smithsonian, 60 Garden Street, Cambridge, MA 02138, USA
[13] Max-Planck-Institut für Astronomie, Königstuhl 17, D-69117, Heidelberg, Germany
[14] Department of Physics and Astronomy, The Johns Hopkins University, 3400 N. Charles Street, Baltimore, MD 21218, USA
[15] Department of Astronomy and Astrophysics, University of California, Santa Cruz, 1156 High Street, Santa Cruz, CA 95064, USA
[16] NRC Herzberg, 5071 West Saanich Road, Victoria, BC V9E 2E7, Canada
Received 2023 December 20; revised 2024 July 1; accepted 2024 July 22; published 2024 October 25

Abstract

We present the robust selection of high-redshift quiescent galaxies (QG) and poststarburst (PSB) galaxies using ultra-deep NIRCam and MIRI imaging from the JWST Advanced Deep Extragalactic Survey (JADES). At $3 < z < 6$, MIRI 7.7 μm imaging provides rest-frame J band, which is commonly used to break the degeneracy between old stellar populations and dust attenuation at lower redshifts. We identify 23 passively evolving galaxies in UVJ color space in a mass-limited ($\log M_\star/M_\odot \geqslant 8.5$) sample over 8.8 arcmin^2. An evaluation of the contribution of the 7.7 μm shows that JADES-like NIRCam coverage (9+ photometric bands) can compensate for lacking the J band at these redshifts; however, more limited three-band selections perform better with MIRI. Our sample is characterized by rapid quenching timescales ($\sim$100–600 Myr) with formation redshifts $z_f \lesssim 9$ and includes a potential record-holding massive QG at $z_{\rm phot} = 5.33^{+0.16}_{-0.17}$ and two QGs with evidence for significant residual dust content ($A_V \sim 1$–2). In addition, we present a large sample of 12 $\log M_\star/M_\odot = 8.5$–9.5 PSBs, demonstrating that UVJ selection can be extended to low mass. An analysis of the environment of our sample reveals that the group known as the Cosmic Rose contains a massive QG and a dust-obscured star-forming galaxy (a so-called Jekyll and Hyde pair) plus three additional QGs within $\sim$20 kpc. Moreover, the Cosmic Rose is part of a larger overdensity at $z \sim 3.7$, which contains 7/12 of our low-mass PSBs. Another four low-mass PSBs are members of an overdensity at $z \sim 3.4$; this result strongly indicates low-mass PSBs are preferentially associated with overdense environments at $z > 3$.

Unified Astronomy Thesaurus concepts: Galaxy evolution (594); High-redshift galaxies (734); Dwarf galaxies (416); Galaxy environments (2029); Galaxy quenching (2040)

1. Introduction

A persistent challenge to a complete picture of galaxy evolution is explaining the cessation of star formation in galaxies. It is one of the most transformational events in the life cycles of galaxies, giving rise to galaxy bimodality (e.g., Kauffmann et al. 2003; Baldry et al. 2004), underpinning the Hubble sequence (Hubble 1926), and creating the distinctly passive populations that inhabit local galaxy clusters (Butcher & Oemler 1978). Yet, we lack a comprehensive picture of the astrophysics that halts galaxy growth (e.g., Man & Belli 2018). Large-scale extragalactic surveys have demonstrated that a number of physical processes are likely at play, impacting preferentially both the most massive galaxies and galaxies in the densest environments (e.g., Peng et al. 2010). However, the relative importance of these quenching processes over cosmic time remains mostly unconstrained, in part due to the difficulty in performing a uniform identification of quiescent galaxies[18] (QGs). Additionally, the environment plays an ever larger role as the growth of cosmic structure proceeds, which

[17] NHFP Hubble Fellow.

[18] In this work, we refer to passively evolving galaxies by the terms QG and PSB galaxy in different contexts for convenience (see Section 4.1); the latter is typically defined spectroscopically as a young passively evolving galaxy with a spectrum still dominated by A-type stars. At the redshifts relevant to this study ($z > 3$), most massive passively evolving galaxies are likely PSBs (D'Eugenio et al. 2020).

creates new challenges as secular quenching and environmental-quenching processes may operate simultaneously.

The remarkable discovery and spectroscopic confirmation of massive QGs beyond $z > 3$ (<2 Gyr after the Big Bang) has now brought us closer to the epoch when QGs first emerged. JWST spectroscopy has enabled new powerful constraints on the timescales over which $z > 3$ QGs form and "quench" (stop forming stars), indicating that some massive galaxies may have formed extremely rapidly (formation era $z > 9$), and quenched their star formation quickly (growth lifetime <200–700 Myr; Nanayakkara et al. 2022; Carnall et al. 2023a; Glazebrook et al. 2023; de Graaff et al. 2024). These timescales and their stellar masses are extreme enough to cause tension with the expectation of typical baryonic growth efficiencies (Labbé et al. 2023; Xiao et al. 2023). Regardless of this tension, given the short cosmic timescales (within the first billion years after the Big Bang), these early quiescent sources represent key opportunities to place constraints on quenching mechanisms in a more straightforward way than at later times. Unfortunately, the majority of spectroscopic studies to date have targeted candidates selected from wide-area surveys with relatively limited and shallow photometric coverage. This has limited detailed characterization of QGs to only the most massive and brightest systems at $z < 4$–5, with gravitational lensing paving the way in enabling spectroscopic analysis at $10 < \log M_\star/M_\odot < 11$ for small lensed and eventually unlensed samples at cosmic noon ($1.5 < z < 3$; e.g., Newman et al. 2018; D'Eugenio et al. 2020; Akhshik et al. 2023; Marchesini et al. 2023; Park et al. 2023). As such, little is known about the evolution and population statistics of old, massive QGs at cosmic noon, nor younger, more recently quenched poststarbursts (PSBs; see footnote 18; e.g., Glazebrook et al. 2017; Schreiber et al. 2018a; Antwi-Danso et al. 2023a; Carnall et al. 2023b; D'Eugenio et al. 2024; Looser et al. 2023; Strait et al. 2023) at redshifts $\gtrsim$3–5. And the lower-mass (log $M_\star/M_\odot < 10$) QG population remains largely unstudied beyond the low-redshift Universe.

The abundance of QGs across cosmic time and their typical timescales for quenching are key constraints on the prevalence of specific quenching mechanisms. In massive galaxies, active galactic nuclei (AGN) are often invoked in simulations to reproduce the bimodality of galaxies (e.g., Somerville & Davé 2015, and references therein), and black hole mass has been shown to be a strong predictor of quiescence (e.g., Bluck et al. 2022; Piotrowska et al. 2022; Bluck et al. 2023). How this proceeds remains unclear, however. Rapid quenching may be induced by strong AGN feedback and outflows (e.g., Peng et al. 2015; Trussler et al. 2020), or more gradual quenching may result from moderate AGN feedback that prevents gas inflows and results in starvation (e.g., Bluck et al. 2022; Piotrowska et al. 2022; Baker et al. 2023a). Similarly, environmental mechanisms capable of quenching galaxies can proceed rapidly ($\sim$ few hundred Myr)—i.e., ram pressure stripping (RPS) of cold, dense gas (Cortese et al. 2021; Boselli et al. 2022)—or more slowly (>1 Gyr), as in the case of starvation and/or RPS of hot halo gas (Larson et al. 1980; Balogh et al. 2000). The environment may also trigger or enhance internal quenching mechanisms through efficiently cutting off gas inflows or through gravitational interactions and/or galaxy mergers (see Alberts & Noble 2022, for a review).

Strong observational constraints on quenching timescales have been hard-won. Observations of the leftover gas reserves in QGs (Bezanson et al. 2019; Whitaker et al. 2021b; Belli et al. 2021; Williams et al. 2021; Suzuki et al. 2022) point to both extremely rapid and effective destruction of star-forming fuel *and* to significant lingering gas reservoirs (French et al. 2015; Rowlands et al. 2015; Alatalo et al. 2016; Suess et al. 2017; Spilker et al. 2022). The reconstruction of star formation histories (SFHs) from detailed rest-frame optical spectroscopy has also proven to provide powerful constraints (Kriek et al. 2016; Glazebrook et al. 2017; Schreiber et al. 2018a; Belli et al. 2019, hereafter B19; Forrest et al. 2020; Suess et al. 2022a; Tacchella et al. 2022b; Kriek et al. 2023; Setton et al. 2024). These approaches, however, are exceedingly costly and yield small samples, making selection of promising targets and supplemental statistical studies with photometric data sets extremely important. With JWST, we are now moving into the high-redshift regime where the limited age of the Universe may ease the interpretation of SFHs. An additional intriguing new opportunity is the possibility of isolating environmental mechanisms through the study of dwarf (log $M_\star/M_\odot < 9$–9.5) galaxies. In the low-redshift Universe, secular quenching in dwarf galaxies is expected to occur over long timescales, with <1% of log $M_\star/M_\odot \sim 8$ galaxies expected to quench without environmental influence (Geha et al. 2012). We are now in a position to test if this is also the case at higher redshifts with JWST.

In this work, we take advantage of ultra-deep JWST/MIRI (Wright et al. 2023) imaging in F770W (reaching 28 mag, 5σ) to supply rest-frame J band at $3 < z < 6$, breaking the degeneracy between old stellar populations and reddening from dust (e.g., Labbé et al. 2005; Williams et al. 2009). We identify signs of quenching in a mass-limited sample down to log $M_\star/M_\odot = 8.5$, assess the robustness of our Hubble Space Telescope (HST)+NIRCam+MIRI selection and the need for the MIRI anchor, and present the properties of QG and PSB galaxies to high redshift and low mass. This work will provide guidance for the wider extragalactic surveys focused on NIRCam, with no or relatively shallow MIRI coverage, such as CEERS (reaching 25.3–26.5 in F770W over $\sim$14 arcmin^2; Yang et al. 2023), COSMOS-Web (24–25 AB in F770W over 0.19 deg^2; Casey et al. 2023), and PRIMER (25.6 AB in F770W over 0.066 deg^2; PI: J. Dunlop, GO 1837). In Section 2, we present the data used in this study, and in Section 3, we present the selection of our mass-limited parent sample and measurement of its properties. Section 4 describes the selection of our QG and PSB samples and how this selection would change given color derived with NIRCam only or with three-band (observed) color selections proposed in the literature. In the discussion (Section 5), we examine the completeness and contamination in our selection (Section 5.1-5.1.2), the nature of our sample (Section 5.2), the relation between quenching in low-mass galaxies and environment (Section 5.3), and the abundance of QGs at high redshift (Section 5.4). Section 6 presents our conclusions. All magnitudes are quoted in the AB system (Oke & Gunn 1983). We adopt concordance cosmology ($\Omega_M = 0.3$, Ω_λ=0.7, $H_0 = 70$ km s^{-1} Mpc^{-1}), and a Kroupa (2001) initial mass function.

2. Data

The primary data set for this work is NIRCam and MIRI imaging from the JWST Advanced Deep Extragalactic Survey (JADES; Eisenstein et al. 2023) in the region where deep MIRI imaging in a single band, F770W, was obtained in parallel with deep NIRCam imaging in 2022 October (PID 1180; PI D. Eisenstein). The MIRI imaging includes four pointings just

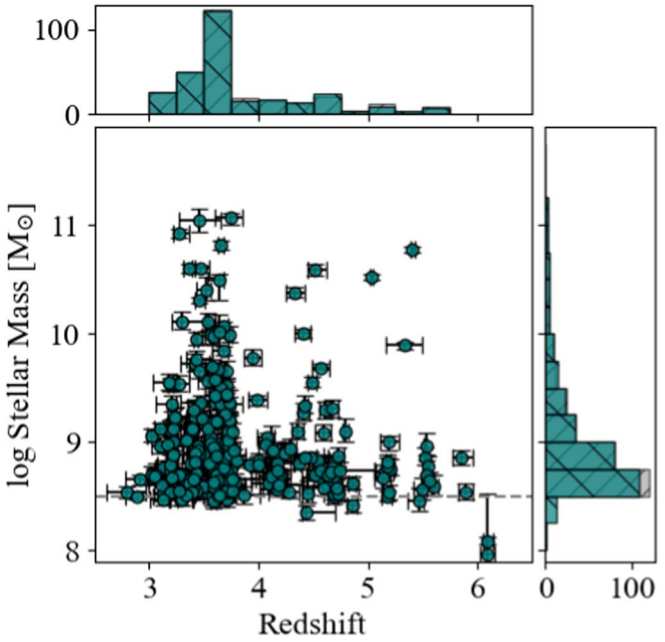

Figure 1. Photometric redshift and stellar mass distribution of the final, mass-selected sample, cut at $\log M_\star/M_\odot \geqslant 8.5$. The main panel shows the properties (green circles) derived from fitting including the F770W data point. The histograms show the distributions with (green solid) and without (gray hatched) the F770W flux density.

south of the Hubble Ultra Deep Field (Beckwith et al. 2006) in GOODS-S and totals 61–94 ks of exposure time per pointing. A majority of the MIRI parallel area ($\sim$8.8 arcmin^2) is covered by JADES medium-depth NIRcam imaging in eight filters (F090W, F115W, F150W, F200W, F277W, F356W, F410M, F444W), with additional partial coverage ($\sim$4 arcmin^2) in F335M (PID 1210; N. Luetzgendorf). A small region ($\sim$1.1 arcmin^2) is additionally covered by F182M, F210M, and F444W imaging from the public First Reionization Epoch Spectroscopic COmpete Survey (FRESCO; Oesch et al. 2023). We further incorporate HST imaging over the full area at 0.4–0.85 μm (F435W, F606W, F775W, F814W, F850LP) from the Advanced Camera for Surveys (ACS) from the deep composite images compiled by the Hubble Legacy Field (Illingworth et al. 2016; Whitaker et al. 2019). The NIRCam data reduction and construction of the JADES HST+NIRCam photometric catalog follow the description in Rieke et al. (2023).

Data processing for the MIRI parallel closely follows the procedure presented in Alberts et al. (2024); a full description of the reduction of the MIRI parallel will be presented in S. Alberts et al. (2024, in preparation). As this work relies heavily on the measurement of accurate colors, we adopt HST and NIRCam photometry extracted from images convolved to the F444W point-spread function (PSF; FWHM 0.″145). Rather than convolve HST and NIRCam further to the resolution at F770W (0.″26), we rebin and convolve only the F444W image to the MIRI pixel size (0.″06) and PSF[19] using ASTROPY routines `convolve_fft` and `reproject` (Astropy Collaboration et al. 2022). We then measure the F444W − F770W color of sources in the JADES NIRCam detection image (Rieke et al. 2023) in an aperture with diameter $d = 0.''7$ (covering $\sim$65% encircled energy at F770W) with no aperture corrections applied. For $z > 3$ galaxies, we assume that a $d = 0.''7$ aperture is more than sufficient to encompass the entire galaxy given their typical sizes ($R_e \lesssim 0.''25$ at $z \sim 3$–5; Shibuya et al. 2015; Ormerod et al. 2023). For the remainder of this work, unless otherwise specified, we use aperture-corrected HST + NIRCam + MIRI photometry extracted using a $d = 0.''5$ aperture, deriving the F770W in this smaller aperture based on the ($d = 0.''5$ aperture-corrected) total F444W flux and the convolved F444W − F770W color. By doing this, we preserve the advantage of the higher NIRCam resolution by adopting an aperture size appropriate to compact galaxies at high redshift, although still large enough to measure an integrated color robust against potential color gradients.

In total, we have 17 bands of deep photometry covering 0.4–7.7 μm for the majority of our area. The five HST/ACS bands reach 5σ point-source sensitivities of $\sim$28–29 mag, the nine JADES NIRCam bands reach 29–30 mag (in a 0.″2 aperture Hainline et al. 2024), MIRI F770W reaches 27.6–27.9 mag (0.″8 aperture, S. Alberts et al. 2024, in preparation). Over a smaller area, we additionally have FRESCO F182M and F210M, reaching depths of 28.2 mag (0.″3 aperture; Oesch et al. 2023).

3. Sample and Properties

For our parent sample, we build a mass-limited ($\log M_\star/M_\odot \geqslant 8.5$) catalog of $3 < z < 6$ galaxies within the JADES MIRI footprint. To do this, we start with an initial sample of 1350 galaxies with a JADES photometric redshift (see Hainline et al. 2024, for details) measured with EAZY (Brammer et al. 2008) between $z_{\rm phot} = 3$ and $z_{\rm phot} = 6$ and with a $F_{\rm F444W}$ flux density greater than 28.9 mag; this low limit is chosen to ensure completeness down to our mass limit. We perform a first pass of spectral energy distribution (SED) fitting (described in the next section) using JADES HST+NIRCam photometry (Section 2) to measure and make a cut on stellar mass.

3.1. SED Fitting

As our goal is to identify quenched galaxies, we adopt the Bayesian SED fitting code BAGPIPES[20] (Carnall et al. 2018), which has been used extensively in modeling QGs (Carnall et al. 2019b, 2020, 2023a; Hamadouche et al. 2022; Antwi-Danso et al. 2023b; Hamadouche et al. 2023; Kaushal et al. 2023; Leung et al. 2023). Our fits use the default BAGPIPES stellar population models, namely, the 2016 update of Bruzual & Charlot (2003) from Chevallard & Charlot (2016). For the assumed SFH, we adopt a parametric double power law (Carnall et al. 2018, 2019a). By separately treating the rising and falling slopes, a double power-law SFH allows for rapid and recent quenching (Merlin et al. 2018), which is the expected dominant mode of quenching at high redshift, observable in a PSB or young QG phase (e.g., Whitaker et al. 2012; Wild et al. 2016; Rowlands et al. 2018; B19; Park et al. 2023).

Dust attenuation is modeled using Noll et al. (2009) and Salim et al. (2018), which is parameterized as a power-law deviation from the Calzetti et al. (2000) attenuation law. As our sample will contain galaxies ranging from quiescent to dusty

[19] Due to the presence of the cross-artifact in the F560W and F770W bands (Gáspár et al. 2021), we adopt an empirical F770W PSF constructed from high dynamic range imaging of stars taken during JWST commissioning (A. Gaspar 2024, private communication).

[20] BAGPIPES uses the MULTINEST nest sampling algorithm (Feroz et al. 2019) via PYMULTINEST (Buchner et al. 2014).

and star forming, we allow a large variation in the *V*-band attenuation ($A_V = 0$–10). Nebular and continuum emission are included based on the CLOUDY photoionization code (Ferland et al. 2013; Byler et al. 2017) with a fixed ionization parameter ($U = 10^{-3}$) and a stellar birth cloud lifetime of 10 Myr. Stellar and gas-phase metallicity are assumed to be identical, and the metallicity parameter is allowed to vary between 0.2 and 2.5 times solar metallicity. The JADES EAZY photometric redshifts are used as priors, and we impose a 5% error floor on all photometric bands.

With this setup, we fit our initial, flux-limited sample of 1350 galaxies and use the median of the stellar mass posterior distributions to define our $3 < z < 6$ parent sample as mass limited at $\log M_\star/M_\odot \geqslant 8.5$.[21] We identify 304 galaxies above this mass cut in our 8.8 arcmin^2 area; 288 (293) have a signal-to-noise ratio (SNR) $> 5\sigma$ ($>3\sigma$) detection in F770W.

SED fitting is performed twice on the mass-limited parent sample: once with HST+NIRCam photometry only and then again adding in the F770W. Final fits using the HST+NIRCam +MIRI photometry with χ^2_ν greater than 1σ of their expected χ^2 distribution given their degrees of freedom (number of bands minus the number of free parameters) are visually inspected, and seven are rejected: one is a star in GAIA DR2; Gaia Collaboration et al. 2018, one is a probable star with a saturated core, and five are improperly deblended substructures within extended, low-redshift galaxies. We also note double-peaked posteriors for the metallicity in nine high-mass ($\log M_\star/M_\odot > 9.7$) galaxies. As metallicity is not robustly constrained by photometry (Tacchella et al. 2022b; Nersesian et al. 2023), we refit all galaxies above this mass with metallicity fixed to $1/3\,Z_\odot$, appropriate for $\log M_\star/M_\odot \sim 10$ galaxies at $z \gtrsim 3$ (Cullen et al. 2019; Sanders et al. 2021), and fixed to $Z_\odot$ (Maiolino & Mannucci 2019). We adopt the fit that resolves the double-peaked posteriors with the lowest χ^2_ν.[22] The resulting redshift and stellar mass distributions are shown in Figure 1. The histograms show the difference in distributions between the HST+NIRCam and the HST+NIRCam+MIRI fitted redshifts and masses; they are nearly indistinguishable as the redshifts and stellar masses with and without the F770W are in good agreement (see the next section for further discussion). Of our final 297 sources in our parent sample, 96% are fit with $\geqslant$13 bands of photometry. The percentages with medium-band photometry in F182M, F210M, F335M, and F410M are 17%, 16%, 44%, and 100%, respectively.

The BAGPIPES fits provide measurements of basic properties (redshift, stellar mass, colors, specific star formation rate, hereafter SSFR, mass-weighted age) as well as higher-order properties (formation redshift, quenching timescales, see discussion in Section 5.2.1). As was shown in Suess et al. (2022b) using mock recovery tests, basic property measurements of PSB galaxies are robust when using both parametric (delayed-τ models, double power-law models; e.g., Carnall et al. 2019a) and nonparametric (continuity prior; e.g., Leja et al. 2019a) SFHs. Specifically, double power-law SFHs in BAGPIPES were recently shown in Kaushal et al. (2023) to recover late-time SFHs consistent with the nonparametric continuity prior used in the PROSPECTOR modeling code (Johnson et al. 2021) in massive galaxies. Higher order properties are known to be sensitive to the assumed priors, particularly in the case of complex intrinsic SFHs (Suess et al. 2022b; Kaushal et al. 2023); for example, a double power-law SFH cannot capture multiple bursts of star formation, such as expected from a rejuvenation event (Akhshik et al. 2021; Woodrum et al. 2022). The accurate measurement of formation and quenching timescales for QGs using a double power law with BAGPIPES was tested in Carnall et al. (2018; see also Carnall et al. 2019a) against simulated galaxies with a range of SFHs, finding median systematic offsets of 100–200 Myr but significant scatter.

3.2. Measuring Stellar Masses with MIRI

With our parent sample, we now investigate whether the addition of deep MIRI F770W photometry significantly changes the inferred stellar masses by providing rest-frame near-infrared constraints and mitigating uncertainties from, e.g., dust attenuation or recent star formation. Even with JWST, the ideal coverage past the peak in stellar emission at $\gtrsim$1 μm (rest-frame) redshifts out of NIRCam at $z \gtrsim 3$. Recent work presented by the CEERS team (Papovich et al. 2023) found that MIRI coverage at F560W and F770W significantly reduced the stellar masses of high-redshift galaxies with sparse $<$1 μm (rest-frame) coverage. Potential drivers of this difference are young stellar populations, which have been shown to easily outshine older populations in spatially resolved and integrated studies (e.g., Baker et al. 2023b; Giménez-Arteaga et al. 2023), and galaxies where emission lines boost emission in broadband filters (Arrabal Haro et al. 2023; Endsley et al. 2023; Pérez-González et al. 2023; Tacchella et al. 2023; but see Desprez et al. 2024).

In Figure 2, we show the comparison of stellar masses measured with and without the F770W band (tracing rest-frame 1.9–1.1 μm at $z = 3$–6). We find a remarkably tight correlation across our mass range, with a scatter of $\sim$0.07 dex. This tight, linear correlation is also seen in the redshifts derived with and without MIRI, which has a 1σ scatter of 0.14. We note that we also find good agreement between the BAGPIPES-derived redshifts and our EAZY redshift priors, with a scatter of 0.19. This agreement is likely due to the 8–11 bands of deep NIRCam coverage; the dense coverage including one to four medium bands with high SNR can accurately establish the shape of the optical continuum without a strong susceptibility to emission lines boosting one to two filters (Arrabal Haro et al. 2023; Desprez et al. 2024). This holds even for our most dust-obscured sources (up to $A_V \sim 4$), in contrast with the stronger differences ($\sim$0.6 dex) in stellar mass found when selecting specifically for the so-called HST-dark galaxies at $z > 3$ (Williams et al. 2023). Similar to this work, weak to no difference is found for most $z \sim 8$ galaxies in the JADES MIRI parallel (J. Helton et al. 2024, in preparation), which are expected to generally be blue star-forming galaxies (SFGs) with little dust (e.g., Stanway et al. 2005; Wilkins et al. 2011).

4. Quiescent Galaxy Candidates with Deep MIRI

4.1. Rest-frame UVJ Colors and Specific-SFR Thresholds

The commonly used *UVJ* color selection for massive QGs (e.g., Williams et al. 2009; Whitaker et al. 2011; Muzzin et al. 2013; Straatman et al. 2014, 2016) hinges on having a long-

[21] The lowest-mass galaxies in our parent sample reach a minimum flux of 35 nJy, 3.5x our initial flux cut and 7x the F444W point-source sensitivity, with SNR $\gtrsim$ 10. Assuming stellar mass scales with the rest-frame 1 μm, it is likely our parent sample is fully mass limited. However, full completeness testing is beyond the scope of this work.

[22] The revised fits are all subsolar except in the case of 179465 and 172799, which have $\log M_\star/M_\odot \sim 11$.

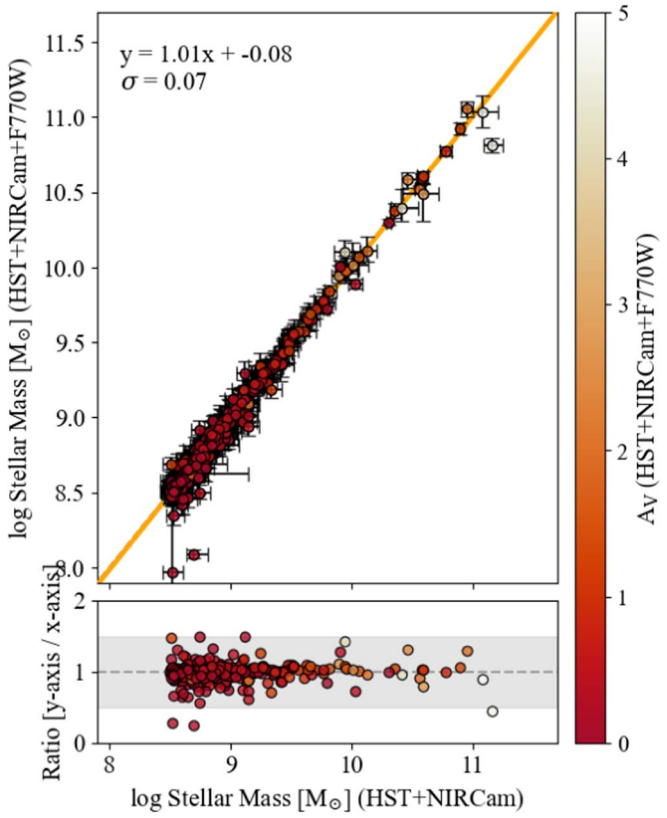

Figure 2. Comparison of the stellar mass measurements down to log $M_\star/M_\odot = 8.5$ with and without the F770W data point. The color bar indicates A_V. The vast majority, save for a few at $A_V \gtrsim 2$, are well fit by a linear relation (orange line) with a scatter of 0.07 dex.

wavelength anchor, typically rest-frame J band, to break the degeneracy between stellar age and dust reddening. Prior to JWST, access to this anchor quickly redshifted out of sensitive ground-based and HST photometry and was either supplied by the lower resolution, lower sensitivity Spitzer/IRAC bands or extrapolation from SED fitting. Unfortunately, such sparse coverage and/or extrapolation is known to greatly increase contamination from reddened star-forming galaxies at $3 < z < 6$ (e.g., Antwi-Danso et al. 2023b).

JWST improves selection in multiple ways: denser wavelength coverage of the rest-frame near-infrared, higher sensitivity, which can greatly decrease uncertainties when measuring rest-frame colors (Merlin et al. 2018), and, with MIRI imaging, interpolation (rather than extrapolation) to rest-frame J band. In Figure 3, we show the inferred rest-frame $U-V$ and $V-J$ colors for our mass-limited parent sample, measured from our SED modeling, in two redshift bins. The median uncertainties in the colors are $\sigma(U-V) = 0.05(0.04)$ and $\sigma(V-J) = 0.05(0.06)$ at $z = 3$–4 ($z = 4$–6). Closed symbols are derived from fits including F770W, which are tied by dotted lines to open symbols derived from fits excluding F770W. In most cases, colors derived with and without F770W are in good agreement; the median color shifts in $U-V$ are negligible, while the color shifts in $V-J$ are largely comparable to the measurement uncertainties for $8.5 \leqslant \log M_\star/M_\odot < 9.5$ and are small (median $\Delta(V-J) = 0.06$) but systematically redder for $\log M_\star/M_\odot > 9.5$ (Figure 3, right, inset).

Initial QG selection is done using the *UVJ* selection (purple lines) from Antwi-Danso et al. (2023b), empirically derived using pre-JWST observations at $3 < z < 4$. The purple dashed line (Figure 3, right) denotes an additional padded region (Antwi-Danso et al. 2023b); such extensions of *UVJ* are commonly used to capture even younger passively evolving populations as we move to higher redshifts (Schreiber et al. 2018a; Carnall et al. 2020; Marsan et al. 2022). We supplement this with the selection proposed in Belli et al. 2019 (B19), which removes the $U-V$ boundary entirely to identify young PSBs (see also Forrest et al. 2020; Marsan et al. 2022). For ease of discussion, we will hereafter refer to candidates that are *UVJ*-selected as QGs and candidates that are selected via the B19 line only as PSB galaxies. We note, however, that these distinctions are for convenience, and most massive passively evolving galaxies at $z > 3$ likely fall under classical, spectroscopy-based definitions of PSB (i.e., spectral features that indicate A-type stars dominate; D'Eugenio et al. 2020).

At $3 < z < 4$, we identify five QGs via *UVJ*-selection. At $4 < z < 6$, we find an additional two in the main *UVJ* selection and three in the padded region. In the B19 PSB region, we find an additional 17 at $3 < z < 4$ and one at $4 < z < 6$. Image cutouts, SEDs, SSFR posteriors, and SFHs for these sources can be seen in Figures 4 and A1–A2. Upon inspection, incorporating the F770W into the SED modeling, and therefore the color measurements, results in only one minor change in classification at $z > 4$. JADES 172811 moves from the edge of the main *UVJ* region to the edge of the padded region when MIRI is added (Figure 3, right). However, visual inspection reveals that the F770W flux is blended with a close neighbor (Section 5.3), and so, we adopt the classification and modeling without the F770W data point. We further inspect the SEDs, images, and SFHs (Figure A2) of the other two sources (JADES 5070 and 65559) in the *UVJ* padded region and find that their SEDs are not well fit by our model ($\chi^2_\nu \sim 20$), and their UV emission and SSFRs ($\log [\mathrm{SSFR\ yr^{-1}}] \gtrsim -10$) are consistent with some residual star formation. We add them to our tentative PSB sample. Hereafter, we will indicate "QG" or "PSB" when using specific galaxy IDs.

4.1.1. Determining Selection Robustness

When selecting QGs, *UVJ* and other color selections can be less sensitive to the assumptions that go into SED modeling than other methods, provided you can measure accurate rest-frame colors. On the other hand, this selection comes with a loss of information. For example, it has been shown that *UVJ* colors are not correlated with SSFR below $\log (\mathrm{SSFR\ yr^{-1}}) \sim -10.5$ (Leja et al. 2019b); robustly measuring SSFR requires additional far-UV or mid-IR observations. As we have such observations, we test the robustness of our candidates by making a redshift-dependent cut on the measured SSFR

$$\mathrm{SSFR} < \frac{0.2}{t_{\mathrm{obs}}}, \tag{1}$$

where SSFR is measured using the star formation rate (SFR) averaged over the last 100 Myr (SFR_{100}), and t_{obs} is the age of the Universe at the observed redshift (e.g., Fontana et al. 2009; Gallazzi et al. 2014; Pacifici et al. 2016; Carnall et al. 2018; Merlin et al. 2018). Although more model-dependent, this approach takes full advantage of our extensive photometry, including coverage of the rest-UV via HST F435W, F606W, F775W, and F814W.

To label a QG candidate as robust, we require that >97.5% of its SSFR posterior (referred to as $\mathrm{SSFR}_{97.5\%}$ hereafter) is

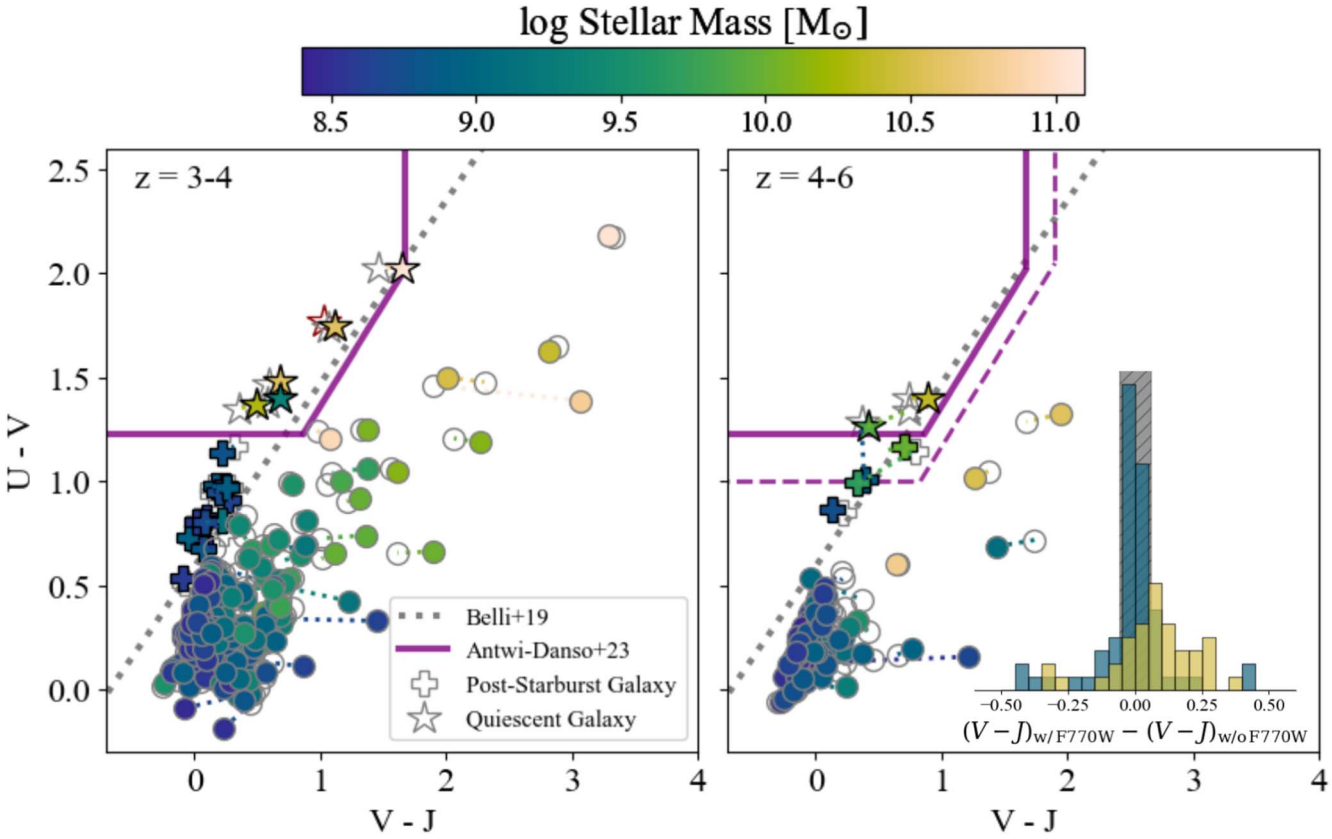

Figure 3. The rest-frame *UVJ* colors of log $M_\star/M_\odot \geqslant 8.5$ galaxies in the JADES MIRI parallel footprint at $z = 3$–4 (left) and $z = 4$–6 (right). The stars, pluses, and circles indicate QG candidates, PSB candidates, and SFGs, respectively. Closed symbols colored by stellar mass are colors derived from SED modeling including the F770W data point. Open gray symbols are colors derived from fits excluding F770W. The connecting lines show where sources move in *UVJ* space when MIRI is added. The red open star is the close companion source to JADES 172799 (172799b; Section 5.3). The purple solid (dashed) line shows the main (expanded) *UVJ* selection region for QGs from Antwi-Danso et al. (2023b). The gray dotted line is the selection from B19, which extends past the standard $U - V$ boundary. The inset histogram shows that the color shifts are consistent within the measurement uncertainties (gray hatched region) for log $M_\star/M_\odot = 8.5$–9.5 (blue), but show a small systematic shift redward at higher masses (orange).

below this evolving threshold. Four of our QGs (176606, 175039, 16170 at $3 < z < 4$, and 35453 at $4 < z < 6$) pass this threshold. One additional QG (172799) also passes the threshold; however, its SED and placement in the *UVJ* diagram suggest significant dust content (see Section 5.2.3). We label this candidate as tentative. QG 178211, mentioned in Section 4.1 as being blended at F770W by a neighbor, meets the $SSFR_{97.5\%}$ threshold only when MIRI is excluded and is also labeled tentative. Two other QGs (172809 and 170932) are labeled as tentative as they only clear ∼50%–80% of their SSFR posteriors below the threshold. These sources and their measured properties are listed in Table 1.

Of our 16 PSB candidates, six meet a relaxed threshold of $SSFR_{50\%}$; these six make up our robust PSB candidates and the remainder our tentative PSB candidates. Their properties are listed in Table 2. We note that slight adjustments of the B19 line in *UVJ* space would result in new PSBs being selected and others being deselected. We revisit this in Section 5.

4.1.2. Candidate Samples Summary

Our robust sample of QGs spans log $M_\star/M_\odot \sim 8.8 - 10.6$ in stellar mass. In Figure 4, it is clear that their SEDs and cutouts have weak to no UV emission, consistent with their low SSFRs (log [SSFR yr^{-1}] $\lesssim -11.5$). Our highest-redshift candidate, QG 35453 at $z_{phot} = 5.3^{0.16}_{0.17}$, would be the highest-redshift *massive* QG known to date if spectroscopically confirmed. None of these candidates have been previously identified.

Our four tentative QG candidates are more of a mixed bag (Figure 4). As stated above, QG 172799 has an unusual SED suggestive of high dust content (see Section 5.2.3) and is additionally part of a large, compact structure that includes a massive, dusty galaxy as well as QG 172809 and PSB 173604. QG 178211 is also spatially located near this group but at a higher redshift. This will be explored in Section 5.3. As these neighbors may have minor to moderate blending at F770W, we verify that their fits and measured properties with and without F770W are consistent within the uncertainties, with the exception of QG 178211 (see Section 4.1). Our last tentative candidate, QG 170932, has a more typical SED and no neighbors, and its failure to meet our $SSFR_{97.5}$ cut is likely due to our use of SFR averaged over 100 Myr rather than a more instantaneous measure.

Our PSB candidates (Table 2), on the other hand, range from log $M_\star/M_\odot \sim 8.6$–10. They typically have more UV emission and blue $U - V$ colors. Our robust PSB subsample (Figure A1) is characterized by low SSFRs (log [SSFR yr^{-1}] $\lesssim -11$) and SFHs that rapidly rise and fall (see Section 5). Our tentative PSBs have higher SSFRs ($-10 \gtrsim$ log [SSFR yr^{-1}] $\lesssim -9$) consistent with residual or ongoing star formation and more extended SFHs (Figure A2). In Section 5, we discuss whether the tentative PSBs should be considered candidates for quenched galaxies.

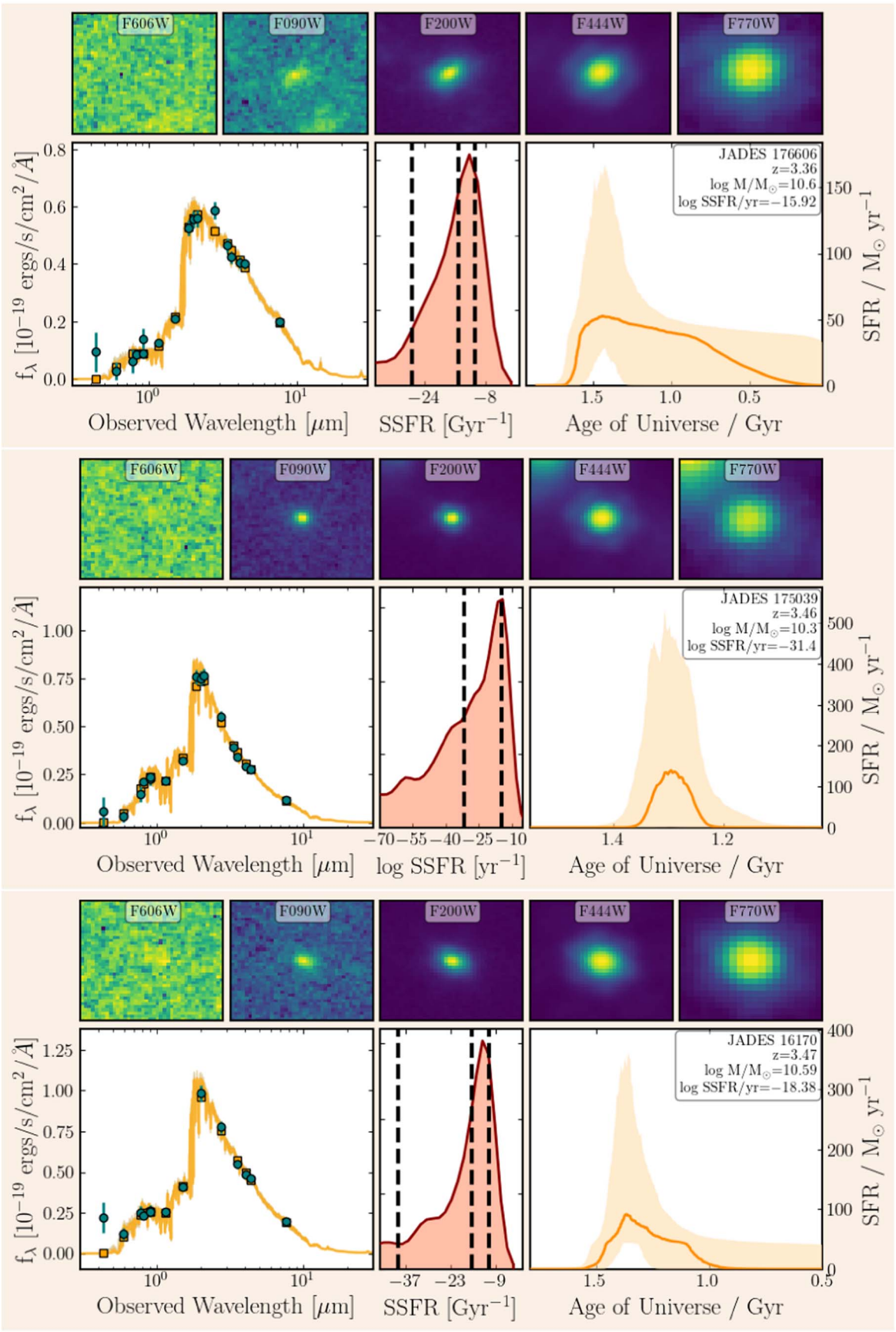

Figure 4. Properties of the *UVJ*-selected quiescent galaxies. Top row for each source: F606W, F090W, F200W, F444W, F770W cutouts, 1.″2 on a side. Bottom row for each source: the SEDs (left), SSFR posterior distributions (middle), and SFHs (right). Robust candidates are highlighted with tan backgrounds.

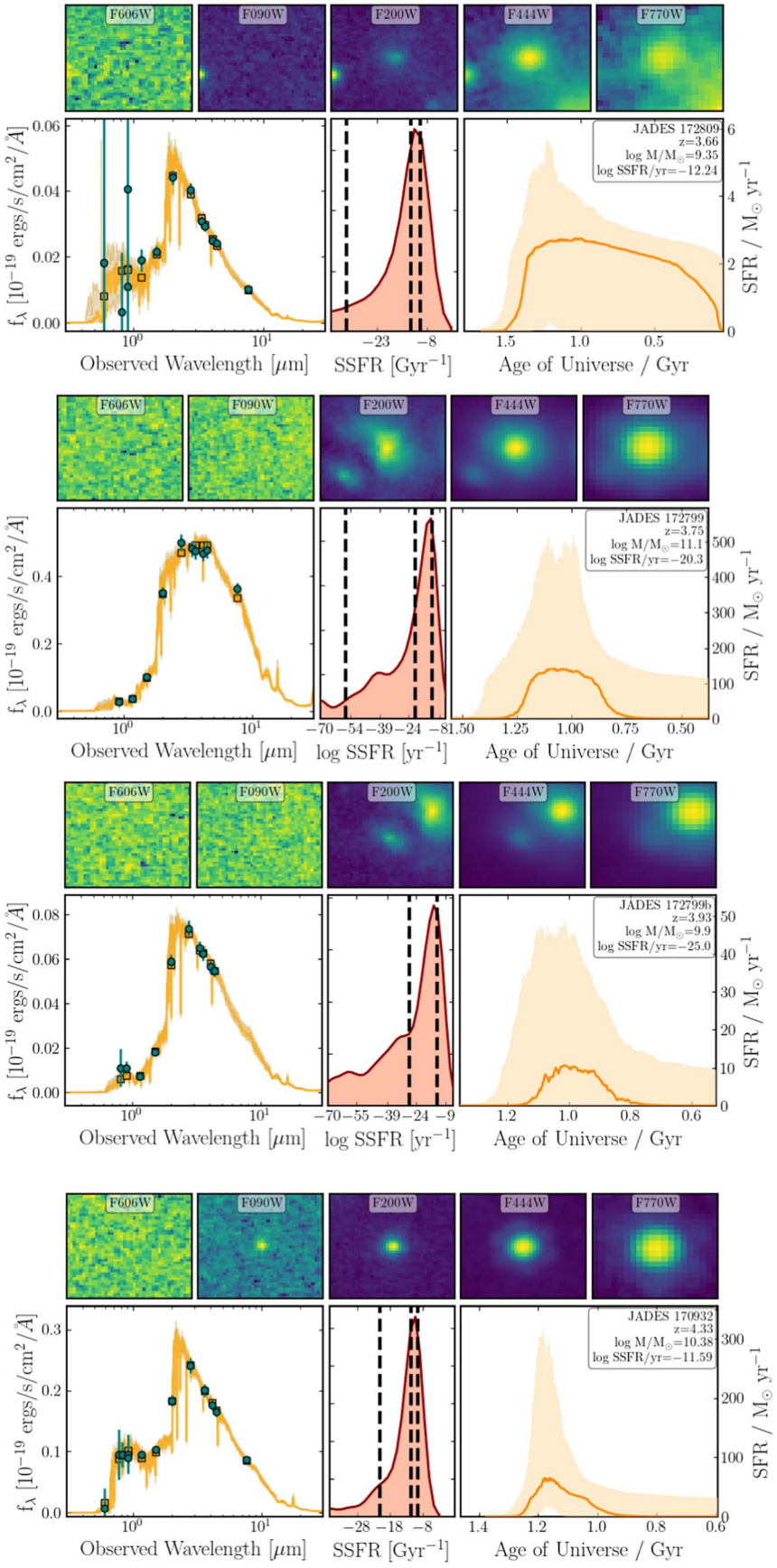

Figure 4. (Continued.)

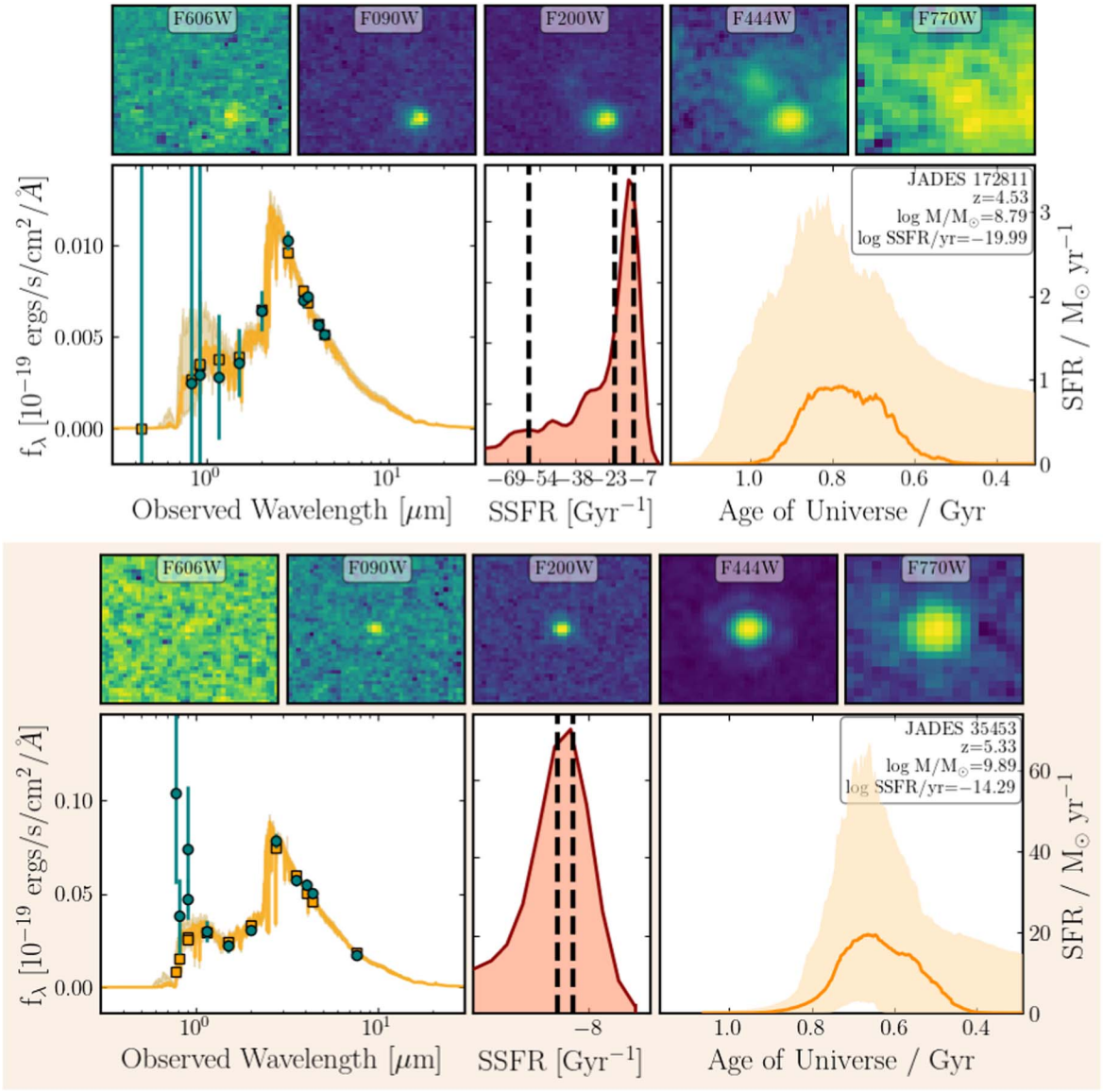

Figure 4. (Continued.)

4.2. Observed-frame Three-band Color Selection with JWST

With our QG and PSB candidates identified, we now look at (observed-frame) color selection of passively evolving galaxies with JWST, before returning to our sample's properties in Section 5. At $z > 3$, the rest-frame J-band redshifts to >5 μm; as such, pre-JWST QG color selection was limited to the relatively shallow Spitzer/IRAC 5.8 and 8.0 μm filters or to extrapolation via SED fitting in order to obtain this long-wavelength anchor. The effects of extrapolation on UVJ color selection are discussed in detail in Antwi-Danso et al. (2023b), which found that the omission of rest-frame J-band data at $z > 2$ results in up to 1 mag of scatter in the $V - J$ color, as well as some scatter in $U - V$ due to the rest V band moving past observed H band. The result is a contamination rate of false positives equal to the selection of true QGs by $z = 3.5$.

4.2.1. NIRCam Only

Extrapolation is similarly necessary with an NIRCam-only UVJ selection at $z > 3$, although with the distinction that NIRCam here provides sensitive imaging via four to six filters longward of the 4000 Å break at $z = 3$–6. This places stronger constraints on the continuum slope than previous K-band +IRAC1+IRAC2 combinations used at high redshift, minimizing for example, uncertain slopes due to strong emission lines. In addition, our sources have photometry in one to four medium-band filters (F182M, F210M, F335M, F410M); medium bands (and dense wavelength coverage in general) have been shown to be beneficial in reducing systematics through ground-based J, H, and K medium bands at lower redshifts (Marchesini et al. 2010; Whitaker et al. 2010; Spitler et al. 2014; Tomczak et al. 2014; Straatman et al. 2016; Esdaile et al. 2021). In Figure 3, we show that adding the F770W to the full JADES HST+NIRCam photometry produces relatively small shifts in the measured rest-frame colors. This results in our classifications of QGs and PSBs remaining the same with and without the F770W data point.

This successful extrapolation of the continuum using HST +NIRCam alone to disentangle old stellar populations from dust-reddened star formation is likely a function of our robust

Table 1
UVJ-selected Quiescent Galaxy Candidates

ID	R.A.	Decl.	z	$\log M_\star/M_\odot$	$U-V$	$V-J$	$\mathrm{Age_{MW}}$ (Gyr)	z_f	z_q	Δt_q[a] (Gyr)	τ_q[a]
					Robust						
176606	53.076502	−27.864167	$3.36^{+0.06}_{-0.05}$	$10.6^{+0.04}_{-0.04}$	$1.75^{+0.03}_{-0.03}$	$1.11^{+0.05}_{-0.05}$	$0.64^{+0.37}_{-0.27}$	$4.9^{+1.47}_{-1.47}$	$3.8^{+0.24}_{-0.24}$	0.4	0.3
175039[b]	53.082581	−27.866812	$3.46^{+0.05}_{-0.04}$	$10.3^{+0.02}_{-0.02}$	$1.37^{+0.02}_{-0.01}$	$0.5^{+0.04}_{-0.04}$	$0.51^{+0.04}_{-0.04}$	$4.7^{+0.16}_{-0.16}$	$4.5^{+0.19}_{-0.19}$	0.1	0.1
16170[b]	53.083613	−27.887586	$3.47^{+0.08}_{-0.08}$	$10.6^{+0.03}_{-0.03}$	$1.48^{+0.03}_{-0.02}$	$0.68^{+0.05}_{-0.06}$	$0.51^{+0.41}_{-0.09}$	$4.8^{+1.58}_{-1.58}$	$4.1^{+0.24}_{-0.24}$	0.2	0.2
35453	53.057030	−27.874375	$5.33^{+0.16}_{-0.17}$	$9.9^{+0.03}_{-0.04}$	$1.26^{+0.04}_{-0.03}$	$0.41^{+0.06}_{-0.07}$	$0.47^{+0.15}_{-0.11}$	$8.6^{+2.09}_{-2.09}$	$6.6^{+0.95}_{-0.95}$	0.2	0.3
					Tentative						
172809[c,d]	53.047848	−27.870220	$3.66^{+0.20}_{-0.23}$	$9.4^{+0.03}_{-0.04}$	$1.4^{+0.08}_{-0.06}$	$0.68^{+0.08}_{-0.09}$	$0.84^{+0.17}_{-0.38}$	$6.4^{+0.99}_{-0.99}$	$4.2^{+0.48}_{-0.48}$	0.6	0.4
172799[c,d]	53.047509	−27.870503	$3.75^{+0.11}_{-0.15}$	$11.1^{+0.05}_{-0.06}$	$2.03^{+0.05}_{-0.05}$	$1.65^{+0.07}_{-0.07}$	$0.63^{+0.26}_{-0.22}$	$5.7^{+1.33}_{-1.33}$	$4.7^{+0.70}_{-0.70}$	0.3	0.2
172799b[c,d]	53.047627	−27.870576	$3.93^{+0.11}_{-0.11}$	$9.9^{+0.05}_{-0.04}$	$1.77^{+0.06}_{-0.06}$	$1.03^{+0.12}_{-0.10}$	$0.57^{+0.25}_{-0.12}$	$5.9^{+1.23}_{-1.23}$	$5.2^{+0.59}_{-0.59}$	0.1	0.1
170932	53.062269	−27.875047	$4.33^{+0.09}_{-0.09}$	$10.4^{+0.05}_{-0.04}$	$1.4^{+0.04}_{-0.04}$	$0.89^{+0.07}_{-0.06}$	$0.27^{+0.41}_{-0.08}$	$5.3^{+1.96}_{-1.96}$	$4.8^{+0.28}_{-0.28}$	0.2	0.1
172811[e]	53.048109	−27.870184	$4.53^{+0.22}_{-0.20}$	$8.8^{+0.05}_{-0.04}$	$1.29^{+0.09}_{-0.09}$	$0.36^{+0.13}_{-0.09}$	$0.54^{+0.21}_{-0.16}$	$7.1^{+1.77}_{-1.77}$	$6.0^{+0.93}_{-0.93}$	0.2	0.2

Notes.
[a] The quenching timescale, Δt_q, is the difference between the time at which a galaxy quenched (t_q) and its formation time (t_f). $\tau_\mathrm{q} \equiv \Delta t_\mathrm{q}/t_\mathrm{q}$ is the normalized quenching timescale. See Section 5.2.1.
[b] Member of the $z \sim 3.4$ overdensity.
[c] Members of the Cosmic Rose.
[d] Member of the $z \sim 3.7$ overdensity (see Sections 5.3, Appendix B for further details on the overdensities).
[e] Measured parameters from fit not including F770W.

photometric coverage from UV-near-infrared, allowing for accurate photometric redshifts and colors. To test this, we look at the color selection presented in Long et al. (2023), which combines three NIRCam bands to bracket the 4000 Å break (F150W and F277W) and measure the continuum slope longward of the break (F277W and F444W). For this test, we apply a conservative cut on the F150W flux of 28 mag, as suggested in Long et al. (2023), to the JADES catalog within the MIRI footprint and measure the (observed) F150W − F277W and F277W − F444W colors (Figure 5). We note that the typical SNR (≫50) of the JADES NIRCam photometry used in this test allows us to measure very accurate observed NIRCam colors. Using the main Long et al. (2023) color selection, 5/5 of our QG candidates (above the flux limit) plus one PSB candidate (65559) are selected, plus an additional five sources not in our candidate list. Two are low-mass galaxies not in our parent sample at $z \sim 1$. The remaining three are at $z > 3$ with log (SSFR yr^{-1}) $\gtrsim -9$. This implies a minimum 60% contamination rate of $z > 3$ interlopers; we have not accounted for contamination due to photometric scatter that will be present in lower-SNR observations. The extended Long et al. (2023) color cuts, intended to capture more of the young PSB population, select an additional 22 galaxies (16 at $z_\mathrm{phot} > 2.5$), only three of which are selected by the B19 line.

4.2.2. NIRCam Plus MIRI

Can reintroducing the long baseline with MIRI reduce the contamination rate in an observed-frame three-band color selection? Based on forward modeling of simulated QGs in the FLARES zoom-in simulation (Lovell et al. 2021; Vijayan et al. 2021), Lovell et al. (2023) developed color selections for $z > 5$ involving the F770W or F1280W MIRI filters combined with two NIRCam bands. We apply their F150W − F770W versus F444W − F770W selection in Figure 5 (right) with the F150W magnitude cut at 28 mag as in the previous section plus a cut on F770W at 25 mag, the depth of the MIRI F770W parallels for COSMOS-Web (Casey et al. 2023). This selection recovers 4/4 QG candidates above the flux limits and only introduces one contaminant at $z_\mathrm{phot} > 2.5$ (and 21 low-mass contaminants at $z_\mathrm{phot} < 2.5$, which are not in our parent sample). With the caveat that we are working with a small area and sample, this suggests that a quenched galaxy selection is more robust given dense wavelength coverage with NIRCam longward of the 4000 Å break *or* F444W plus moderate depth MIRI imaging at F770W, given a rough cut in redshift is possible. We note that Lovell et al. (2023) found that using F1280W as the longwave anchor produced a selection with >80% in completeness and purity.

5. Discussion

In this work, we have selected $3 < z < 6$ QGs using *UVJ* color space and PSB galaxies using the B19 selection, with robustness criteria for quiescence based on a redshift-dependent threshold in SSFR. This selection takes full advantage of 11–14 bands of high-SNR (≫50) HST+NIRCam photometry plus a long-wavelength anchor at rest-frame 1–2 μm provided by ultra-deep MIRI F770W photometry (although as discussed in Sections 4.1, our sample is the same with and without this anchor). In this section, we take a closer look at the properties of our sample.

Figure 6 presents our QG and PSB candidates relative to the main sequence (MS; e.g., Popesso et al. 2023, and references therein), i.e., $\Delta\mathrm{MS} = \log(\mathrm{SFR}/\mathrm{SFR_{MS}})$, where the SFR is the median posterior of $\mathrm{SFR_{100}}$ provided by BAGPIPES SED fitting, and $\mathrm{SFR_{MS}}(z, M_\star)$ is the SFR of an MS galaxy at a given redshift and stellar mass from Popesso et al. (2023), a study that covers our full mass range. As expected from our evaluation of their SSFRs (Section 4.1), our QG candidates fall well below the MS (≫1 dex). Gratifyingly, 15/16 PSB candidates selected in color space—10 of which are labeled tentative as they do not meet the $\mathrm{SSFR_{50\%}}$ requirement—also fall significantly below the MS (by $\gtrsim$0.6–1 dex), and only one is an obvious contaminant on the MS, which we discard. This supports that extending the *UVJ* diagonal past the traditional $U-V$ boundary (B19) can select young PSBs, even at low stellar mass. The $U-V$ colors of our PSBs extend down to

Table 2
B19-selected Poststarburst Candidates

ID	R.A.	Decl.	z	$\log M_*/M_\odot$	$U-V$	$V-J$	$\mathrm{Age_{MW}}$ (Gyr)	z_f	z_q	Δt_q[a] (Gyr)	τ_q[a]	ΔMS
					Robust							
177522[b]	53.082093	−27.862845	$3.46^{+0.19}_{-0.14}$	$8.9^{+0.04}_{-0.04}$	$0.97^{+0.05}_{-0.04}$	$0.26^{+0.06}_{-0.05}$	$0.25^{+0.12}_{-0.05}$	$4.1^{+0.24}_{-0.24}$	$3.8^{+0.25}_{-0.25}$	0.2	0.1	< -2
171534[c]	53.079921	−27.870211	$3.67^{+0.11}_{-0.14}$	$8.9^{+0.04}_{-0.04}$	$0.98^{+0.04}_{-0.03}$	$0.17^{+0.07}_{-0.07}$	$0.28^{+0.07}_{-0.04}$	$4.4^{+0.23}_{-0.23}$	$4.1^{+0.21}_{-0.21}$	0.1	0.1	< -2
170254[c]	53.060745	−27.876153	$3.68^{+0.11}_{-0.18}$	$8.6^{+0.04}_{-0.05}$	$0.83^{+0.06}_{-0.09}$	$0.09^{+0.11}_{-0.07}$	$0.2^{+0.05}_{-0.04}$	$4.2^{+0.17}_{-0.17}$	$3.9^{+0.25}_{-0.25}$	0.1	0.1	< -2
173604[d,c]	53.046729	−27.869632	$3.92^{+0.10}_{-0.17}$	$8.8^{+0.04}_{-0.03}$	$1.14^{+0.07}_{-0.06}$	$0.22^{+0.09}_{-0.07}$	$0.46^{+0.21}_{-0.10}$	$5.4^{+0.61}_{-0.61}$	$4.8^{+0.46}_{-0.46}$	0.2	0.1	< -2
79086	53.044180	−27.842933	$4.74^{+0.32}_{-0.24}$	$8.7^{+0.08}_{-0.06}$	$0.87^{+0.10}_{-0.09}$	$0.13^{+0.14}_{-0.11}$	$0.22^{+0.14}_{-0.06}$	$5.8^{+0.71}_{-0.71}$	$5.1^{+0.54}_{-0.54}$	0.2	0.1	< -2
					Tentative							
181568[b]	53.085809	−27.857762	$3.28^{+0.05}_{-0.05}$	$8.7^{+0.04}_{-0.04}$	$0.8^{+0.03}_{-0.02}$	$0.08^{+0.05}_{-0.05}$	$0.19^{+0.08}_{-0.04}$	$3.7^{+0.15}_{-0.15}$	…	…	…	–1.1
172306[b]	53.049332	−27.872567	$3.34^{+0.21}_{-0.15}$	$8.6^{+0.04}_{-0.05}$	$0.91^{+0.07}_{-0.07}$	$0.27^{+0.09}_{-0.10}$	$0.69^{+0.30}_{-0.36}$	$5.0^{+1.05}_{-1.05}$	…	…	…	–1.2
174413[b]	53.082623	−27.868384	$3.55^{+0.08}_{-0.13}$	$9.2^{+0.03}_{-0.03}$	$0.81^{+0.03}_{-0.02}$	$0.21^{+0.04}_{-0.05}$	$0.19^{+0.05}_{-0.03}$	$4.0^{+0.12}_{-0.12}$	…	…	…	–1.0
174444[e]	53.078690	−27.868339	$3.56^{+0.10}_{-0.12}$	$8.6^{+0.04}_{-0.04}$	$0.81^{+0.03}_{-0.02}$	$0.02^{+0.05}_{-0.04}$	$0.22^{+0.08}_{-0.03}$	$4.1^{+0.16}_{-0.16}$	…	…	…	–1.2
174098[e]	53.075869	−27.868852	$3.62^{+0.05}_{-0.07}$	$8.9^{+0.03}_{-0.02}$	$0.73^{+0.02}_{-0.01}$	$-0.04^{+0.03}_{-0.02}$	$0.17^{+0.02}_{-0.02}$	$4.1^{+0.06}_{-0.06}$	…	…	…	–1.1
172569[e]	53.051312	−27.872026	$3.62^{+0.11}_{-0.12}$	$9.0^{+0.04}_{-0.05}$	$0.98^{+0.03}_{-0.04}$	$0.24^{+0.05}_{-0.06}$	$0.3^{+0.21}_{-0.07}$	$4.4^{+0.43}_{-0.43}$	…	…	…	–1.4
40882[c]	53.065272	−27.869663	$3.81^{+0.08}_{-0.06}$	$8.8^{+0.06}_{-0.05}$	$0.67^{+0.04}_{-0.14}$	$0.07^{+0.10}_{-0.07}$	$0.23^{+0.12}_{-0.06}$	$4.4^{+0.38}_{-0.38}$	…	…	…	–0.6
5070[e]	53.092006	−27.903137	$4.41^{+0.07}_{-0.07}$	$10.0^{+0.04}_{-0.03}$	$1.17^{+0.03}_{-0.03}$	$0.7^{+0.09}_{-0.07}$	$1.03^{+0.06}_{-0.08}$	$13.2^{+1.96}_{-1.96}$	…	…	…	–1.3
65559[e]	53.041051	−27.854478	$4.57^{+0.08}_{-0.08}$	$9.7^{+0.03}_{-0.02}$	$0.99^{+0.02}_{-0.02}$	$0.34^{+0.05}_{-0.04}$	$0.95^{+0.05}_{-0.07}$	$12.6^{+1.34}_{-1.34}$	…	…	…	–1.4

Notes.
[a] The quenching timescale, Δt_q, is the difference between the time at which a galaxy quenched (t_q) and its formation time (t_f). $\tau_q \equiv \Delta t_q / t_q$ is the normalized quenching timescale. See Section 5.2.1.
[b] Member of the $z \sim 3.4$ overdensity.
[c] Member of the $z \sim 3.7$ overdensity (see Sections 5.3, Appendix B for further details on the overdensities).
[d] Members of the Cosmic Rose.
[e] Sources are poorly fit with our model ($\chi^2_\nu \sim 20$).

0.5 mag, which is consistent with the colors modeled for rapid quenching (via a top-hat SFH) of dust-free star-forming galaxies presented in Merlin et al. (2018). Additionally, we find that galaxies in the Long et al. (2023) NIRCam color selection that are not in our sample largely fall within the scatter of the MS (Figure 6), consistent with our supposition that they are contaminants (Section 4.2.1).

The remainder of our discussion will go as follows: in the next section, we dive deeper into the completeness and purity of our selection. In Section 5.2, we discuss QG and PSB properties and highlight individual sources; in Section 5.3, we present evidence of an association between overdense environments and our sample down to low mass in a confluence of galaxies known as the Cosmic Rose (Eisenstein et al. 2023) and other overdensities; and finally, in Section 5.4, we examine the number density of QGs suggested by our sample.

5.1. UVJ *Selection with JADES: Completeness and Contamination*

5.1.1. *Completeness*

The expected completeness (and contamination) rate of *UVJ* selection has varied in the literature when calibrated against other measures of quiescence. Part of this has been shown to arise from systematic offsets in the measured rest-frame colors in different data sets (Kawinwanichakij et al. 2016), and part arises from potential quiescent populations that have colors outside of the typical *UVJ* selection (Schreiber et al. 2018a).

In this work, we have adopted the *UVJ* selection presented in Antwi-Danso et al. (2023b). Other common selections (Williams et al. 2009; Whitaker et al. 2011; Muzzin et al. 2013; Carnall et al. 2018) would recover the same sample within the 1σ color uncertainties. We have tested this selection after the fact using a redshift evolving SSFR threshold (Equation (1)), finding that 6/8 (8/8) of our *UVJ*-selected QG candidates have 97.5% (50%) of their SSFR posterior distribution below this threshold. We likewise find no candidates with low SSFR that are not *UVJ* or B19-selected, in agreement with some previous studies (Pacifici et al. 2016; Carnall et al. 2018).

In contrast, Schreiber et al. (2018a)—using a photometric sample of 24 candidate QGs at $3 < z < 4$, supplemented with MOSFIRE *H* and *K* spectra for half the sample—found that 40% of candidates with low SSFRs (10x below the MS) were not found by *UVJ* color selection, but instead inhabited space below (labeled "young quiescent," partially overlapping the B19 selection) and to the right (labeled "dusty quiescent") of the traditional region. We do not find populations redder than the *UVJ* or B19 selection through either our SSFR criteria or comparison to the MS (Figure 6). Carnall et al. (2023a) likewise found disagreement with the QG selection presented in Schreiber et al. (2018a) in a subsample covered by CEERS; our work supports their supposition that JWST data greatly improve the measurement of colors and SSFRs, particularly in dusty sources, reconciling the *UVJ* and SSFR selections.

This agreement was not necessarily expected to hold as we move into these high redshifts, however. In this regime, galaxies are more likely to be low metallicity (e.g., Cullen et al. 2019), and this has been predicted to slow the development of the red colors necessary for *UVJ* selection (potentially on timescales longer than the age of the Universe at the observed redshift; Tacchella et al. 2018). Quiescent/PSB galaxies observed at $z > 3$ are also necessarily younger, which motivates the B19 selection for PSBs and the padded region for *UVJ*-selection at $z > 4$ (Antwi-Danso et al. 2023b). Alternative color selections (Antwi-Danso et al. 2023b; Gould et al. 2023; Kubo et al. 2023) have also been explored to try to capture this young population. To

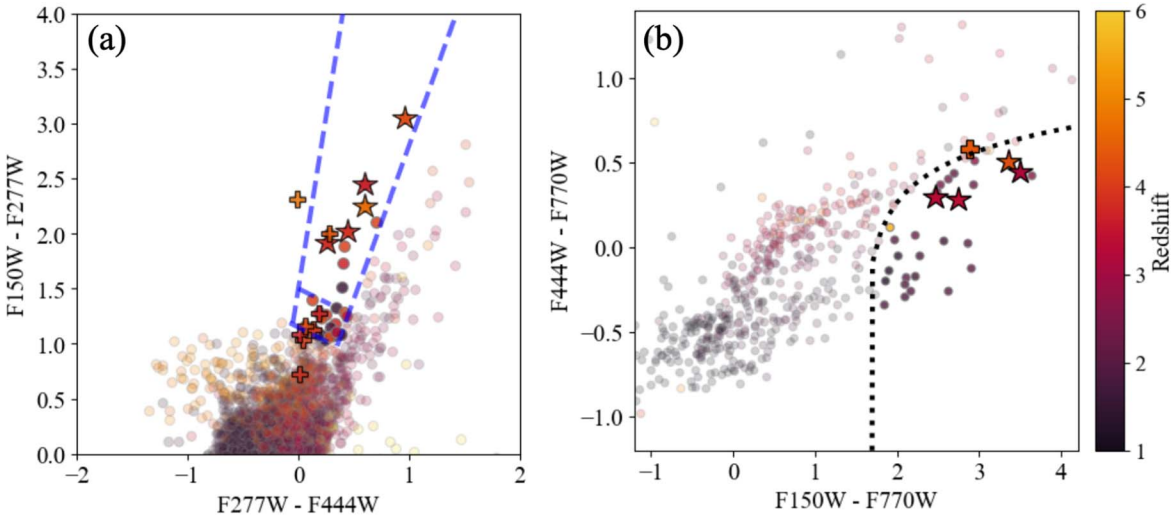

Figure 5. (a) JWST three-band color selection using NIRCam F150W, F277W, F444W from Long et al. (2023) for galaxies with F150W brighter than 28 AB. The blue dashed lines show the QG selection criteria, with an extension toward bluer F150W − F277W colors to capture more young PSBs. (b) The three-band color selection using F150W, F444W, F770W from Lovell et al. (2023) with F150W < 28 and F770W < 25 AB. The black dotted line shows their suggested selection. In both panels, data points are colored by redshift, and the stars and pluses denote the QG and PSB candidates in this study; circles show other galaxies. Given a rough redshift cut of $z_{\rm phot} = 2.5$, we find minimum contamination rates of 60% for the Long et al. (2023) selection and 25% for the Lovell et al. (2023) selection.

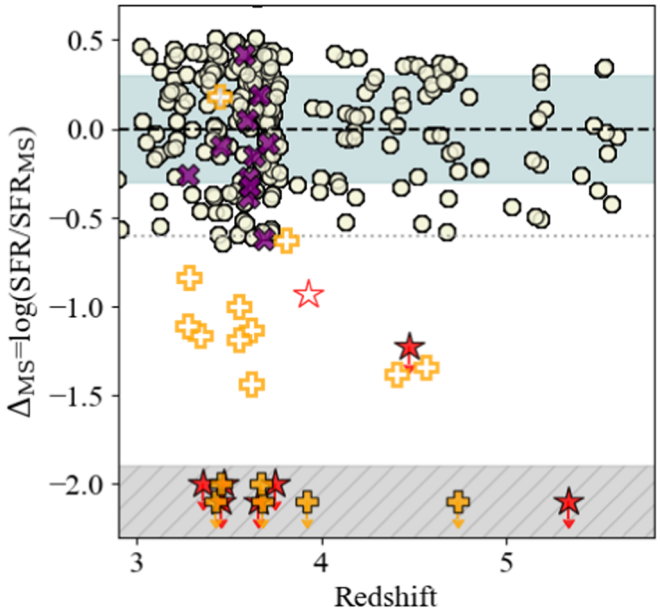

Figure 6. Our mass-limited parent sample relative to the MS from Popesso et al. (2023) as a function of redshift. Red stars (orange pluses) are our QG (PSB) candidates. The red open star is the close companion source to JADES 172799 (172799b; Section 5.3). Solid plus signs indicate our primary PSB sample, while open symbols are the secondary sample. Only one PSB is a contaminant on the MS. White circles are galaxies in our parent sample not selected as QG or PSB. Purple x's are galaxies selected by the Long et al. (2023) NIRCam color selection (Section 4.2.1) that are not in our sample.

test whether *UVJ*-selection is missing young QGs, we consider one additional color selection, $(ugi)_s$, presented in Antwi-Danso et al. (2023b). Designed to mitigate the issues arising from extrapolation to *J* band through new, synthetic *ugi* filters, this color selection is expected to pick out QGs 250 Myr before they enter *UVJ* space as it is optimized to be able to select bluer Balmer breaks. However, we find that, while $(ugi)_s$ color selection is very effective at identifying our main QG candidates, it does not identify any new candidates for young QGs or our PSB sample. The latter is expected as $(ugi)_s$ was designed to maximize purity and minimize contamination from dusty SFGs, which makes it less sensitive to the blue PSB colors short of the break (Antwi-Danso et al. 2023b).

From the above, we conclude that there are no obvious sources of incompleteness in our *UVJ*-selected sample. Issues such as the effects of low metallicity on QG colors remain, however, and will require spectroscopic studies with JWST to resolve.

5.1.2. Contamination

Pre-JWST, the *UVJ* color space for QGs was known to be contaminated at the ∼10%–30% level (Belli et al. 2017; Fang et al. 2018; Merlin et al. 2018; Díaz-García et al. 2019; Leja et al. 2019b); at $z \sim 3$–4, Schreiber et al. (2018a) found this contamination to be dominated by dusty galaxies at low redshifts with poor photometric redshift solutions and strong line emitters. Now, with JWST, and particularly in this work with our 11–14 bands of high-SNR medium and broadband NIRCam+MIRI photometry, we can largely mitigate these contaminants by providing good sampling on the continuum longward of the 4000 Å break, including rest-frame *J* band, accurately measuring photometric redshifts, identifying emission lines, and breaking the degeneracy between stellar age and dust attenuation. This was forecasted in Merlin et al. (2018), which measured the *UVJ* colors for mock catalogs based on CANDELS catalogs using the CANDELS photometric filters and then again with JWST filters. This comparison demonstrated that the addition of JWST photometry greatly reduced the scatter from measurement uncertainties, and in addition, it predicted a much cleaner separation of QGs and SFGs in *UVJ* space, with very few galaxies encroaching on the diagonal *UVJ* boundary. Given this reduction in scatter from measurement uncertainties, one might instead expect that *intrinsic* scatter such as due to complex SFHs or galaxies caught in a transition phase could instead crowd the *UVJ* boundaries. Although our sample is small, we see evidence for a relatively clean separation along the diagonal *UVJ* selection, which is where the slow-quenching evolutionary tracks presented in B19 would be expected to enter. This supports that rapid quenching

is the dominant mode at high redshift in massive galaxies (Whitaker et al. 2012; Wild et al. 2016; Rowlands et al. 2018; B19), as they are not spending much time in a transition phase such as the green valley at $z > 3$. This clean separation suggests that our main *UVJ* selection has low to no contamination. For our PSB sample, this clean separation is not seen. Nevertheless, we find that our PSB list captures all galaxies in our parent sample significantly below the MS, with only one contaminant on the MS. This suggests that this selection from B19, optimized for lower-redshift, higher-mass galaxies, is promising for high-redshift, low-mass PSBs.

5.2. Quenched Galaxies at z = 3–6

5.2.1. Quenching Timescales

From the modeled SFHs, we can estimate properties that broadly describe the life cycles of our QG and PSB samples, including mass-weighted age, formation time, and quenching timescales (Tables 1–2). As in Section 3.1, we caution that these measurements are known to be sensitive to the choice of priors (Suess et al. 2022b; Kaushal et al. 2023), and we limit our comparisons below to observational studies with similar prior assumptions. Our QG and PSB candidates span ∼200–800 Myr in mass-weighted age, corresponding to formation redshifts of $z_f \sim 4$–9.[23] We show the formation time of our robust samples relative to the observed redshift in Figure 7 and compare to the CEERS sample analyzed using similar SED modeling in Carnall et al. (2023a). Split by redshift, our QGs at $3 < z < 4$ have $4.5 \lesssim z_f \lesssim 6.5$, comparable to CEERS. As expected given downsizing and their low masses ($\log M_\star/M_\odot \lesssim 9.5$), the majority of our robust PSBs observed at $3 < z < 4$ have slightly later formation times of $4 \lesssim z_f \lesssim 5.5$.

Unlike the CEERS sample, however, which found that QGs observed at $4 < z < 5$ have formation redshifts $9 < z_f < 12$, our two massive QGs at $z > 4$ formed later at $5 < z_f < 9$. Carnall et al. (2023a) noted that finding such high formation redshifts but no QG observed at $z > 5$ was unexpected. Later formation times such as we find here are in line with predictions from the EAGLE hydrodynamical cosmological simulation (Crain et al. 2015; Schaye et al. 2015) and FLARES, which predict that QGs (defined as $\mathrm{SSFR} < 0.1\,\mathrm{Gyr}^{-1}$) with $z_f \geqslant 10$ should be observed at $z \geqslant 6$ (Lovell et al. 2023). Such extreme early formation timescales as found in Carnall et al. (2023a) may be linked to the extreme massive galaxy candidates being uncovered by JWST (e.g., Glazebrook et al. 2023) and, if confirmed, could place strong constraints on mechanisms for quenching, such as the onset for feedback from supermassive black holes, which drives quenching in the EAGLE and FLARES simulations.

To examine the timescales associated with quenching, we adopt z_q as defined in Carnall et al. (2018) as the redshift at which the current SFR falls to <10% of the time-averaged SFR across the full SFH and calculate $\Delta t_q \equiv t_q - t_f$ and $\tau_q \equiv \Delta t_q / t_q$ (Carnall et al. 2018; Tacchella et al. 2022a); the latter accounts for the difference in dynamical timescales when comparing across a wide range in redshift. As shown in Tables 1–2, our QGs quench on relatively rapid quenching timescales ($\Delta t_q \sim 100$–600 Myr), while our robust PSBs show a narrower range of 100–200 Myr. The quenching timescales for the tentative PSBs are unconstrained, perhaps due to residual star formation. The quenching of galaxies is thought to occur

[23] We exclude 5070 and 65559 from consideration here due to their relatively poor fits (Section 4.1).

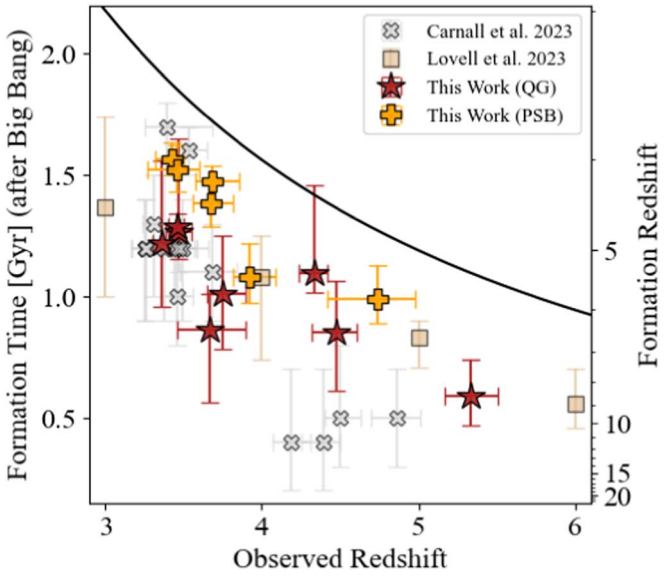

Figure 7. The formation time (since the Big Bang) of our QG (red stars) and primary PSB (orange pluses) candidates as a function of the redshift at which they are observed. The right *y*-axis shows the corresponding formation redshift. The black line shows the age of the Universe at the observed redshift. We compare to the CEERS sample (gray crosses) from Carnall et al. (2023a) and the median timescales from the EAGLE and FLARES simulations (tan squares; Lovell et al. 2023).

through multiple pathways (e.g., Carnall et al. 2018, 2019a; Tacchella et al. 2022a; Hamadouche et al. 2023; B19), which, as demonstrated in Carnall et al. (2018), is reflected in the distribution of τ_q. That work found that τ_q for QGs at $z < 4$ forms three peaks, which was interpreted as three distinction modes of quenching: a rapid rise in star formation followed by rapid quenching ($\tau_q \sim 0.1$, prominent at $z > 2$), a more extended SFH history followed by relatively rapid quenching ($\tau_q \sim 0.4$, dominant at $z \sim 1$–2), and a slow-quenching mode that appears at $z < 1$ ($\tau_q \sim 0.6$). Our QG sample spans the τ_q values of the first and second pathways, which can be visualized in their SFHs in Figure 4. On the other hand, all of our robust PSBs display a relatively uniform rapid rise in star formation followed by rapid quenching (Figure A1).

5.2.2. Quenching in Low-mass Galaxies

Using the B19 extension of PSB selection in *UVJ* space, we have selected 14 PSBs that live significantly below the MS (Figure 6), six of which are supported by SED modeling to have low SSFRs (our robust subsample; Table 2). Although the B19 selection was developed for intermediate-redshift, high-mass galaxies, the majority of our PSBs have log $M_\star/M_\odot \sim 8.5$–9, 1–2 orders of magnitude below the B19 sample. This results undoubtedly in part from our smaller search volume, but nevertheless, it highlights the existence of a new population of high-redshift, low-mass passively evolving galaxies now being revealed with JWST (e.g., Looser et al. 2023; Strait et al. 2023; Cutler et al. 2024). As seen in Section 7 and Figure A1, the SFHs of the robust PSB subsample are consistent with a rapid rise in star formation, followed by rapid quenching. The mechanism behind quenching in low-mass galaxies, even at low- and intermediate-redshifts, is still undergoing intense debate. Our PSBs are too massive to be candidates for UV-background quenching (Efstathiou 1992), but lower mass than the threshold for mass-driven secular

quenching observed at low redshifts (Peng et al. 2010; Geha et al. 2012). The latter has led low-mass quenched galaxies to be associated with environmental quenching; however, the story may be more complicated at high redshift. Temporary ("mini") quenching episodes driven by stochastic star formation and AGN feedback have been invoked (Dome et al. 2024) to explain two spectroscopically confirmed fast-quenching, low-mass galaxies at $z \sim 5$–7 (Looser et al. 2023; Strait et al. 2023). This is plausible as the shallow potential wells of low-mass galaxies likely make them susceptible to gas loss through outflows and winds (Bullock & Boylan-Kolchin 2017; McQuinn et al. 2019; Gelli et al. 2024). Arguments have long been made that AGN, which can produce stronger feedback than stellar processes, are uncommon in dwarf galaxies (e.g., Trebitsch et al. 2018); however, observational (e.g., Kaviraj et al. 2019; Davis et al. 2022, and references therein) and theoretical (e.g., Silk 2017; Koudmani et al. 2021) evidence is mounting to challenge this view, including at high redshift with JWST (Harikane et al. 2023; Maiolino et al. 2023). However, these miniquenching phases may be exceedingly short (∼20–40 Myr; Dome et al. 2024), which would make them difficult to catch without instantaneous SFR tracers from spectroscopy. In photometric work such as that here, it is common to use tracers that probe SFR over the last ∼100 Myr.

On the other hand, the shallow potential wells of low-mass galaxies are also likely susceptible to environmental mechanisms such as RPS (Cortese et al. 2021; Boselli et al. 2022) in filamentary or group-scale overdensities (e.g., Benítez-Llambay et al. 2013; Bluck et al. 2020; Vulcani et al. 2021; Castignani et al. 2022) or the enhancement of internal quenching mechanisms through increased interactions or mergers (Vijayaraghavan & Ricker 2013; Bahé et al. 2019). The effectiveness and timescales of these processes have proven difficult to assess and are thought to range from rapid (∼100 Myr) to slow (>1 Gyr) depending on local conditions (see Alberts & Noble 2022, for a discussion on environmental-quenching mechanisms). It is thus still a challenge to identify mass quenching versus environmental quenching in a given low-mass galaxy. However, we can make some progress by looking at the demographics of larger samples; in Section 5.3, we examine the local environment of our low-mass PSBs.

5.2.3. Dusty Quiescent Galaxies

The response of galaxy colors to increasing stellar age is known to cause a strong gradient in the region of *UVJ* space used to select QGs, with more recently quenched galaxies moving from the bluer, lower left-hand region to the redder upper right-hand region of the selection as they age (e.g., Whitaker et al. 2012; B19). As argued in Carnall et al. (2020), we can expect the upper half of the *UVJ* selection (associated with ages $\gtrsim$1 Gyr in massive galaxies; B19) to depopulate at $z > 3$ as not enough time has elapsed to produce these red colors via an aging population. Alternatively, such colors at $z > 3$ could be caused by dust,[24] which reddens galaxies along a similar vector. Two of our QG candidates, 176606 and 172799, occupy this space, and their dusty nature is supported visually in their SEDs (Figure 4) and by their measured *V*-band attenuations of $A_V = 1$ and $A_V = 2$, respectively.

While photometric disentanglement of the age–dust degeneracy is notoriously difficult, our photometric sampling including four and two NIRCam medium bands for 176606 and 172799, respectively, gives us confidence that we have selected bona fide candidates for dusty QGs suitable for spectroscopic follow-up. The confirmation of quenched galaxies with residual dust has interesting implications as the typical expectation is that the cold interstellar medium (ISM) has been destroyed, evacuated, or heated in order for galaxies to halt star formation (e.g., Davé et al. 2012; Lilly et al. 2013). Infrared stacking of photometric samples has detected nonnegligible cold (Gobat et al. 2018; Magdis et al. 2021) and warm (Blánquez-Sesé et al. 2023) dust in quiescent populations, albeit at lower redshifts. In addition, a handful of spectroscopically confirmed QGs have direct detections of dust in the far-infrared (Whitaker et al. 2021b; Morishita et al. 2022; Lee et al. 2023). These studies seem to contradict the idea of full destruction of the cold ISM; however, a number of unknowns still prevent firm conclusions, including whether dust can be accreted via minor merging (see, e.g., Caliendo et al. 2021; Woodrum et al. 2022), what dust destruction mechanisms dominate and on what timescales (e.g., Whitaker et al. 2021a), and how our assumptions about dust temperatures in QGs bias our interpretation (e.g., Cochrane et al. 2022). Spectroscopic confirmation of the nature of the $z > 3$ dusty QG candidates presented here would provide valuable constraints given the early epoch.

5.3. Environmental Quenching of Low-mass Galaxies at High Redshift: The Cosmic Rose

Beyond its dusty, yet old nature, QG 172799 is the base of the so-called "Cosmic Rose" (Eisenstein et al. 2023), a visually striking structure composed of two massive red galaxies: QG candidate 172799 and a log $M_\star/M_\odot = 11$ dusty SFG (JADES 172813[25]) with SFR $\sim 730\,M_\odot\,\mathrm{yr}^{-1}$ and $A_V \sim 3.5$.[26] This pair, reminiscent of the Jekyll and Hyde galaxies observed at similar redshifts (Glazebrook et al. 2017; Schreiber et al. 2018b; Kokorev et al. 2023), are surrounded by lower-mass quenched galaxies with similar photometric redshifts (Tables 1–2). In Figure 8, we show the F444W, F200W, F090W red, green, and blue (RGB) image of the Rose, which reveals that 172799 has similar colors as 172809, which we have identified as a log $M_\star/M_\odot = 9.4$, relatively old ($\mathrm{age}_{\mathrm{MW}} \sim 0.6$ Gyr) QG. Both QG candidates are fit with $z_{\mathrm{phot}} \sim 3.7$, which would put them at a physical separation of 11 kpc, significantly less than the distance from the Milky Way to the Magellanic Clouds (∼50 kpc; Fitzpatrick et al. 2002). PSB 173604 sits just northwest of the Rose. The image further reveals a potential third companion not identified by the JADES catalog deblending algorithm. Using a smaller aperture ($d = 0.''3$) to isolate this companion, we measure its HST+NIRCam photometry and perform SED fitting. We do not repeat the fit with F770W as the small separation means this companion is likely significantly blended with 172799 in the MIRI photometry. The companion, which we dub 172799b, has a

[24] Obscured AGN can also cause red optical colors. To rule this out, we searched the catalog from Lyu et al. (2022) for AGN within our parent sample. We find that QG 176606 is AGN, but selected in X-ray and not the mid-infrared. This indicates the AGN is likely not luminous in the optical to mid-infrared. QG 172799 has no indication of AGN. We do not find any other indications of AGN among our QG and PSB samples, although the Lyu et al. (2022) catalog does not cover about a third of our MIRI imaging.

[25] Also known as ALESS009.1, spectroscopically confirmed via CO(4–3) at $z_{\mathrm{spec}} = 3.694$ (Birkin et al. 2021).

[26] Due to its size, the properties reported for JADES 172813 were measured here using a Kron aperture.

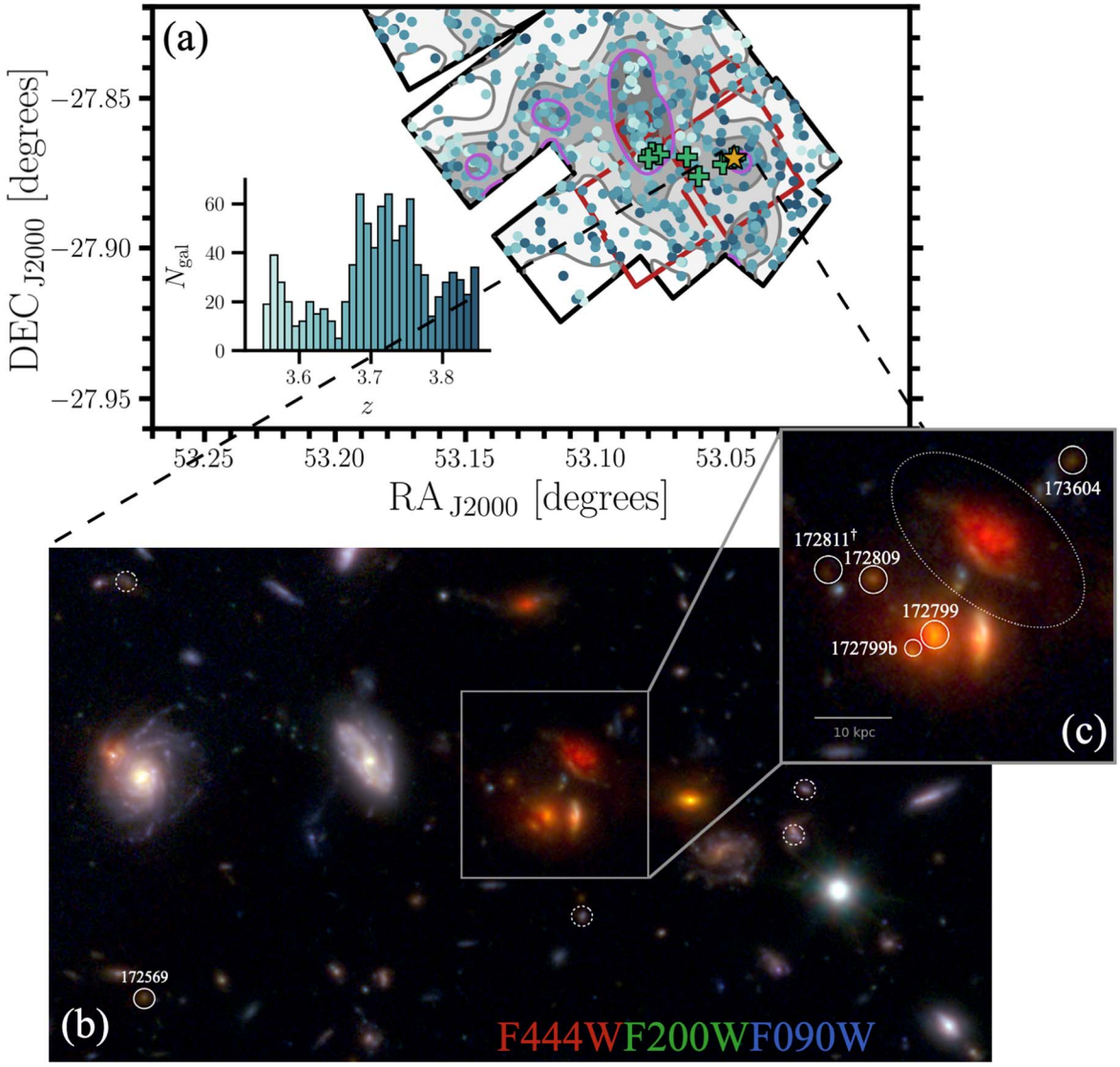

Figure 8. (a) Overdensities of galaxies at $3.55 < z < 3.85$ in the JADES NIRCam (black outline) and MIRI parallel (red outline) field of views. Contours increment by 1σ, with the purple contour outlining 4σ peaks. The yellow star indicates the Cosmic Rose. The green pluses show low-mass PSBs with redshifts consistent with $z = 3.7$. The inset histogram shows the redshift distribution of galaxies in the overdensity. (b) RGB (F444W, F200W, F090W) image of ∼150 kpc around the Cosmic Rose. (c) Zoom-in of the Cosmic Rose. Quiescent and PSB (SFG) galaxies in the $z \sim 3.7$ overdensity are circled with solid (dotted) lines (†172811 is at $z = 4.53$; its proximity to the Rose is a projection effect). QGs and PSBs are labeled.

photometric redshift within 1σ of 172799, has a stellar mass of $\log M_{\star}/M_{\odot} = 9.9$, and meets the criteria for a QG candidate based on *UVJ* and $\mathrm{SSFR}_{97.5}$ (Table 1, Figures 3, 4, 6).

The close proximity of these four quenched galaxies strongly suggests they are related and that their quenching may be environmentally driven. For massive galaxies, environmental quenching is notoriously difficult to disentangle from secular quenching, even in obvious cases of visible signatures such as ram pressure stripped tails or a morphological disturbance from major mergers (Alberts & Noble 2022). For low-mass galaxies, on the other hand, secular quenching mechanisms may act over long timescales, and quenching of dwarf galaxies is known to correlate with overdense environments locally (e.g., Peng et al. 2010, 2012; Bluck et al. 2014, 2016) and at $z \sim 2$ (Ji et al. 2018). As discussed in Section 5.2.2, however, this is an area of intense debate, particularly at high redshift.

Seven of our low-mass PSBs have redshifts consistent with $z = 3.7$ within 2σ. To explore whether this is a coincidence, we look for a larger structure around the Cosmic Rose following the procedure in Sandles et al. (2023; see Appendix B for details). And indeed, we find that there is a $\sim 6\sigma$ overdensity (Figure 8) that peaks just north of the MIRI parallel (α, $\delta = 53.083104$, -27.854775) surrounded by secondary $\sim 4\sigma$ peaks; the Cosmic Rose is located at the edge of a 4.3σ secondary peak with a $\sim 11''$ (80 kpc) radius. This overdensity has been previously identified and was recently confirmed using optical spectroscopy (Shah et al. 2023, and references therein). Overplotted are the locations of the seven low-mass PSBs, which all coincide with regions that are overdense at the 3σ–4σ level.

Among our remaining low-mass PSBs, four have redshifts consistent with $z \sim 3.4$, so we repeat this large-scale structure analysis (Appendix B) and find that these four are also associated with an overdensity at the 3σ–4σ level (see also Shah et al. 2023, and references therein). This means that, out of 12 $\log M_{\star}/M_{\odot} = 8.5$–$9.5$ PSBs, we find that only one (PSB 79086 at $z \sim 4.7$) is not associated with an overdensity. A similar association was found for a spectroscopically confirmed

low-mass (log $M_\star/M_\odot = 8.97$) QG at $z = 2.34$ in JADES (Sandles et al. 2023). These preliminary findings are consistent with a recent result from the CEERS team (Bluck et al. 2024), which examined quenching as a function of the stellar potential (stellar mass divided by half-light radius). They found that stellar potential is the best predictor of quiescence in *massive* galaxies, which they attributed to a tight correlation between stellar potential and black hole mass, making it a tracer of the integrated effects of AGN feedback (D'Eugenio et al. 2024). Conversely, they found stellar potential was not a predictor of quenching in low-mass (log $M_\star/M_\odot = 9$–10) galaxies, which they interpreted as ruling out quenching mechanisms that scale with stellar mass, indirect support of environmental quenching. Although we also do not directly demonstrate environmental quenching in this work, the overwhelming association between low-mass PSBs and overdense environments in our sample at $z > 3$ strongly suggests we focus on establishing or refuting a causal link with environmental quenching in future follow-up.

5.4. The Abundance of Quiescent Galaxies at $3 < z < 6$

Understanding the quenching pathways that dominate galaxy evolution across cosmic time requires tracing the abundances of QGs from their first emergence to later times. Ground-based and HST studies have revealed that QGs at $z \sim 2$–3 are abundant with relatively old stellar ages (up to 1–2 Gyr; Carnall et al. 2020; B19), implying a substantial population already in place at earlier epochs. Pre-JWST estimates of the massive QG number density at $3 < z < 4$, however, vary by over an order of magnitude (Valentino et al. 2023), changing dramatically with the number of filters/wavelength sampling and depth, which highlights the strong dependence of measured abundances on selection functions. In particular, deeper, well-sampled surveys (e.g., space-based or medium-band surveys) tend to identify larger abundances (although these studies are typically limited to smaller areas; Straatman et al. 2014, 2015; Tomczak et al. 2014; Schreiber et al. 2018a; Shahidi et al. 2020) compared to sparsely sampled ground-based (but wide-area) surveys (Muzzin et al. 2013; Davidzon et al. 2017; Valentino et al. 2020; Weaver et al. 2022). Simulations have similarly discrepant results at early times (Cecchi et al. 2019; Girelli et al. 2019; Merlin et al. 2019; Valentino et al. 2023), but this is reflective of the overall poor empirical constraints informing feedback and evolutionary models at $z > 3$ compared to lower redshifts.

In this work, we have the disadvantage of examining a relatively small area (8.8 arcmin^2) but the advantage of exquisitely deep data over observed 0.4–7.7 μm, allowing us to identify a robust, complete photometric sample of QGs with low contamination (Section 5.1). In our two redshift bins, we find number densities of $10^{-3.7\pm0.2}$–$10^{-4.0\pm0.3}$ Mpc^{-3} at $3 < z < 4$ and $10^{-4.4\pm0.3}$–$10^{-4.7\pm0.4}$ Mpc^{-3} at $4 < z < 6$ for our log $M_\star/M_\odot > 9.4$ full and robust *UVJ*-selected QG samples (Figure 9), in good agreement with the recent results from CEERS (Carnall et al. 2023b) and a factor of 2–3x higher than the similarly selected *UVJ* numbers derived from multiple JWST fields, most of which are shallower and have more sparse wavelength coverage (Valentino et al. 2023). This discrepancy could be due to cosmic variance; Valentino et al. (2023) found a factor of 2–3x in field-to-field variation in the number densities in 11 fields ranging from 2–35 arcmin^2 in size. Part of this may be driven by the (often unaccounted for) presence of overdensities, and indeed, as discussed in Section 5.3, we have found that the JADES MIRI parallel contains multiple 3σ–4σ galaxy overdensities (see also Shah et al. 2023). Nevertheless, we suggest that further investigation is needed to test whether these results from small but deep fields indicate that wide, shallow JWST fields are limited in their ability to constrain QG abundances, given a lack of wavelength coverage (no HST or MIRI, sparse NIRCam) and lower significance detections, which increase the uncertainties on measured parameters such as colors or SSFR.

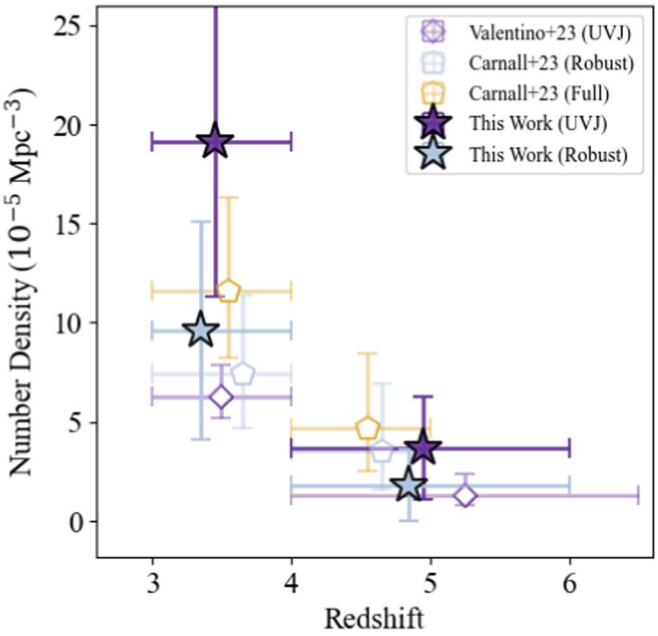

Figure 9. The number density of photometrically selected, massive (log $M_\star/M_\odot \gtrsim 9.5$) quiescent galaxies at $z \sim 3$–6 from our robust (purple stars) and full *UVJ*-selected (pale blue stars) samples. Points are staggered slightly along the redshift axis for visual clarity. We compare to the massive (log $M_\star/M_\odot \gtrsim 9.5$) robust and full samples from Carnall et al. (2023a; pentagons) and the *UVJ*-selected sample from Valentino et al. (2023; diamonds). We find that the abundance of quiescent galaxies in the MIRI parallel agrees with the higher estimates from the deep CEERS survey (Carnall et al. 2023a); however, we caution that our field contains known overdensities (Section 5.3, Appendix B).

6. Conclusions

In this work, we evaluate the selection and properties of QG and PSB galaxies at $3 < z < 6$ in a mass-limited sample (log $M_\star/M_\odot \geqslant 8.5$) using 13–16 bands of HST+NIRCam photometry combined with ultra-deep JADES MIRI F770W imaging, which constrains the rest-frame *J*-band anchor commonly used in the color selection of QGs. SED fitting is done using a double power-law SFH through the BAGPIPES fitting code from which we measure rest-frame colors and galaxy properties. Our main conclusions are as follows:

1. The derivation of photometric redshifts and stellar masses yields consistent results with and without the inclusion of the F770W data point (probing rest-frame 1–2 μm) in the SED fitting (Section 3.2). This is likely the result of the dense wavelength coverage in JADES (8–11 NIRCam bands including one to four medium-band filters per source), which places robust constraints on the continuum longward of the 4000 Å break.
2. The selection of QG and PSB galaxies is done using the standard *UVJ* color diagram plus the extended PSB selection from B19. The robustness of our candidates is

evaluated using a redshift-evolving SSFR cut that takes full advantage of our data set. Over our 8.8 arcmin^2 area, we determine a final sample of four (five) robust (tentative) *UVJ*-selected QGs (Table 1, Figure 4). This corresponds to number densities of massive QGs at $3 < z < 6$ (see Section 5.4) in good agreement with results from JWST surveys to similar depths (Carnall et al. 2023b), with the caveat that our 8.8 arcmin^2 area contains known overdensities (Section 5.3, Appendix B). We additionally identify six (nine) robust (tentative) B19-selected PSBs. We identify only one MS galaxy contaminant in our B19 selection.

3. As with the stellar masses, our sample of QG and PSB candidates is selected equally well with and without the F770W data point, again pointing to the constraining power of the JADES data set. For similar surveys, QG-selection therefore does not require MIRI data at $z > 3$. For fields with sparser JWST wavelength coverage, we test (observed) three-band color selections presented in the literature (Long et al. 2023; Lovell et al. 2023) and find that NIRCam three-band (F150W, F277W, F444W) selection suffers from high ($\gtrsim$60%) contamination. A three-band selection that includes relatively shallow MIRI F770W reduces this contamination rate.
4. Our full QG and PSB galaxies have a range in mass-weighted ages ($\sim$200–800 Myr), corresponding to formation redshifts of $z_f \sim 4$–9. We do not find examples of extremely early ($z = 9$–12) formation times (e.g., Carnall et al. 2023b), despite identifying potentially the highest-redshift massive QG at $z_{phot} \simeq 5.3$.
5. The range in quenching timescales for our sample ($\tau_q \sim 100$–600 Myr) is consistent with rapid quenching pathways. B19-selected robust PSBs have uniformly short quenching timescales (100–200 Myr).
6. Through the B19 selection, we identify a substantial new population of low-mass (log $M_\star/M_\odot = 8.5$–9.5) PSBs with SFHs that are characterized by a rapid rise in star formation followed by rapid quenching (Figures A1–A2) and/or living significantly below the star-forming MS (Figure 6). This demonstrates that *UVJ*-based PSB selection can be extended to low masses.
7. We characterize the nature of the Cosmic Rose (Figure 8), a complex of galaxies dominated by a massive, dusty QG and a massive, dusty SFG at $z \sim 3.7$—a so-called Jekyll and Hyde pair. Three lower-mass QGs are within $\sim$20 kpc of the complex center, indicating likely efficient environmental quenching within this system.
8. An investigation of an extended area reveals that the Cosmic Rose is part of a larger overdensity at $z \sim 3.7$ (see also Shah et al. 2023) that encompasses fully half of our low-mass PSBs. The other half (save one) is located in an overdensity at $z \sim 3.4$. This provides compelling evidence that quenching of log $M_\star/M_\odot \sim 8.5$–9.5 is associated with overdense environments and potentially driven by environmental-quenching mechanisms.

The launch of JWST has opened up new opportunities to trace the evolution of quenching back to the emergence of the first QGs and down to the low-mass regime for which little is known beyond the low-redshift Universe. To take full advantage of this opportunity, we will need both a detailed spectroscopic analysis and robust selection of statistical samples from deep JWST surveys.

Acknowledgments

The authors thank Andras Gaspar for his work on constructing empirical MIRI PSFs and Adam Carnall for discussions about BAGPIPES. The JADES Collaboration thanks the Instrument Development Teams and the JWST instrument teams at the European Space Agency and the Space Telescope Science Institute for the support that made this program possible. The JADES data presented in this paper were obtained from the Mikulski Archive for Space Telescopes (MAST) at the Space Telescope Science Institute. The JADES data release 1 can be accessed via doi:10.17909/8tdj-8n28. STScI is operated by the Association of Universities for Research in Astronomy, Inc., under NASA contract NAS5-26555. Support to MAST for these data is provided by the NASA Office of Space Science via grant NAG5-7584 and by other grants and contracts. The authors acknowledge the use of the lux supercomputer at UC Santa Cruz, funded by NSF MRI grant AST 1828315. This work was performed in part at Aspen Center for Physics, which is supported by National Science Foundation grant PHY-2210452. S.A., J.L., I. S., and G.H.R. acknowledge support from the JWST Mid-Infrared Instrument (MIRI) Science Team Lead, grant 80NSSC18K0555, from NASA Goddard Space Flight Center to the University of Arizona, and S.A., C.C.W., J.M.H., Z.J., K.H., D.J.E., B.D.J., M. R., B.R., and C.N.A.W. acknowledge the JWST/NIRCam contract to the University of Arizona NAS5-02015. The research of C.C.W. is supported by NOIRLab, which is managed by the Association of Universities for Research in Astronomy (AURA) under a cooperative agreement with the National Science Foundation. W.B. and F.D.E. acknowledge support by the Science and Technology Facilities Council (STFC), by the ERC through Advanced grant 695671 "QUENCH," and by the UKRI Frontier Research grant RISEandFALL. S.A. acknowledges support from grant PID2021-127718NB-I00 funded by the Spanish Ministry of Science and Innovation/State Agency of Research (MICIN/AEI/10.13039/501100011033). N.B. acknowledges the Cosmic Dawn Center (DAWN), funded by the Danish National Research Foundation under grant No. 140. A.J.B. acknowledges funding from the "First Galaxies" Advanced Grant from the European Research Council (ERC) under the European Union's Horizon 2020 research and innovation program (grant agreement No. 789056). S.C. acknowledges support by European Union's HE ERC Starting grant No. 101040227—WINGS. E.C.L. acknowledges support of an STFC Webb Fellowship (ST/W001438/1).

Data Availability

The JADES NIRCam imaging (DR1) used in this work can be found on MAST at doi:10.17909/8tdj-8n28. All JADES data releases can be found at https://archive.stsci.edu/hlsp/jades. The JADES MIRI data will be made available in a future release; advanced access may be granted on reasonable request.

Software: ASTROPY (Astropy Collaboration et al. 2013, 2018, 2022), BAGPIPES (Carnall et al. 2018), MULTINEST (Feroz et al. 2019), PYMULTINEST (Buchner et al. 2014).

Appendix A
Poststarburst Candidate Cutouts and SEDs

In this Appendix, we show image cutouts and SEDs for our robust (Figure A1) and tentative (Figure A2) poststarburst candidates selected via the B19 criteria.

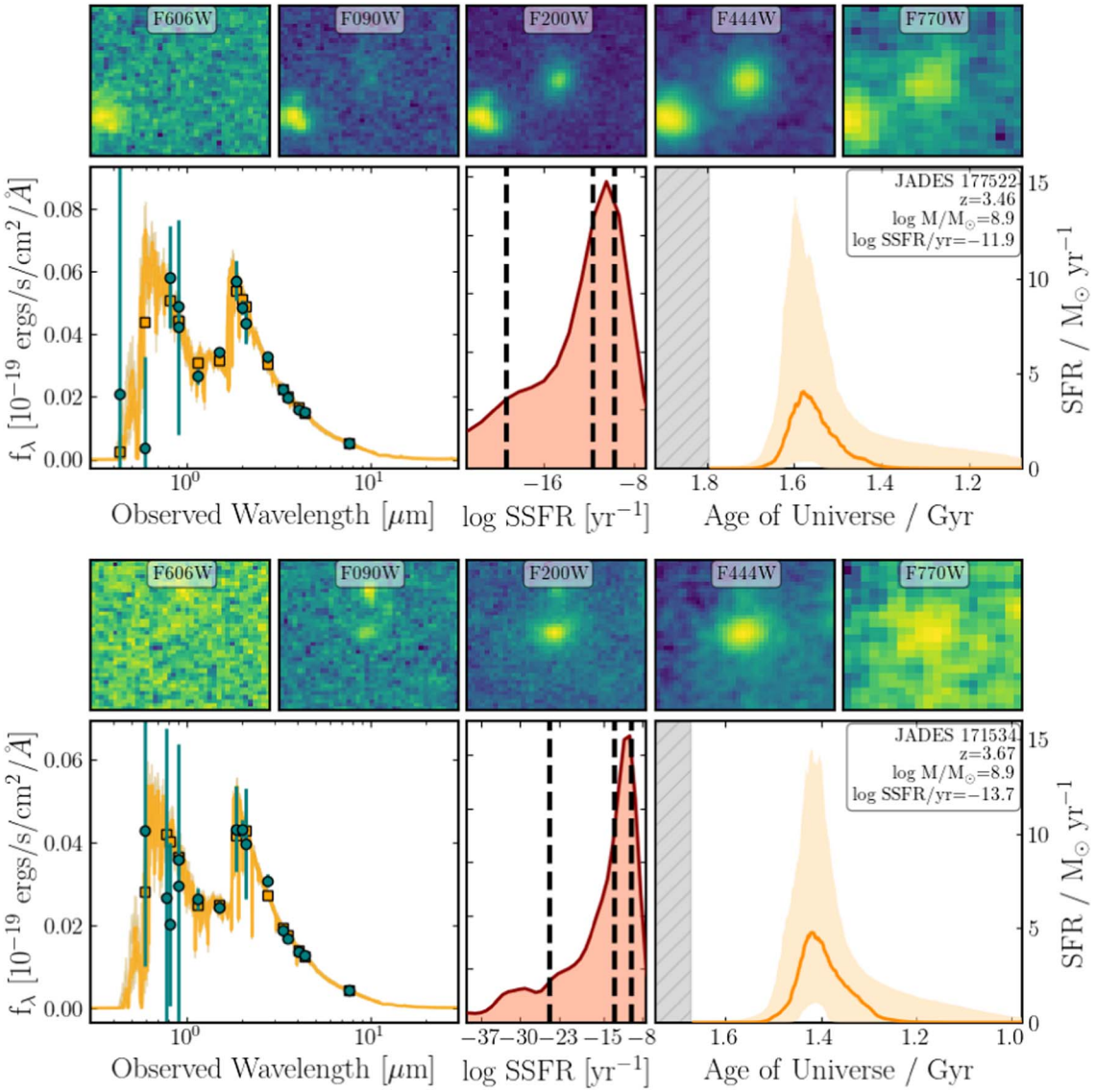

Figure A1. Properties of robust poststarburst galaxies selected via B19. Top rows for each source: F606W, F090W, F200W, F444W, F770W cutouts, 1.″2 on a side. Bottom rows for each source: the SEDs (left), SSFR posterior distributions (middle), and SFHs (right).

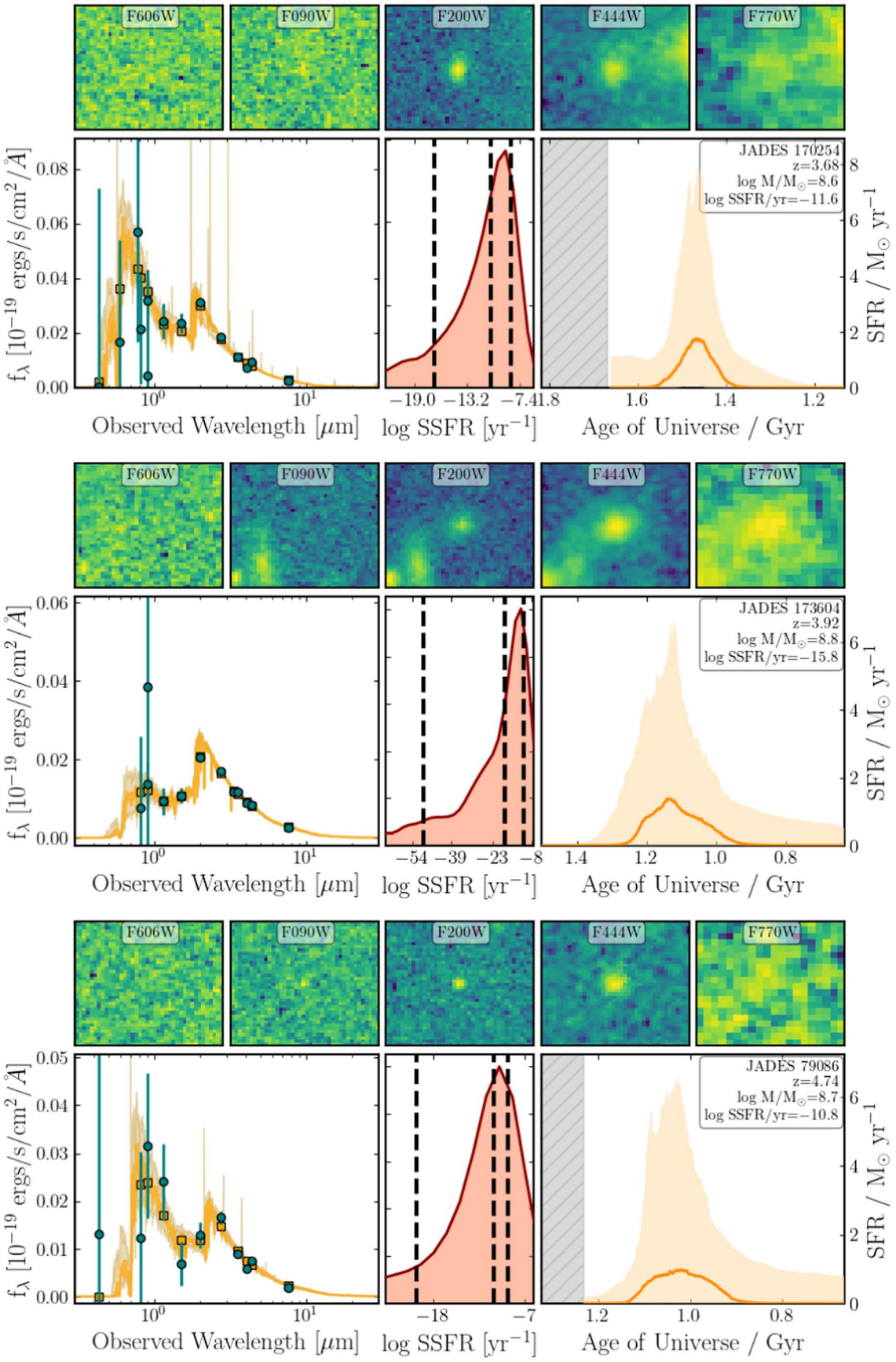

Figure A1. (Continued.)

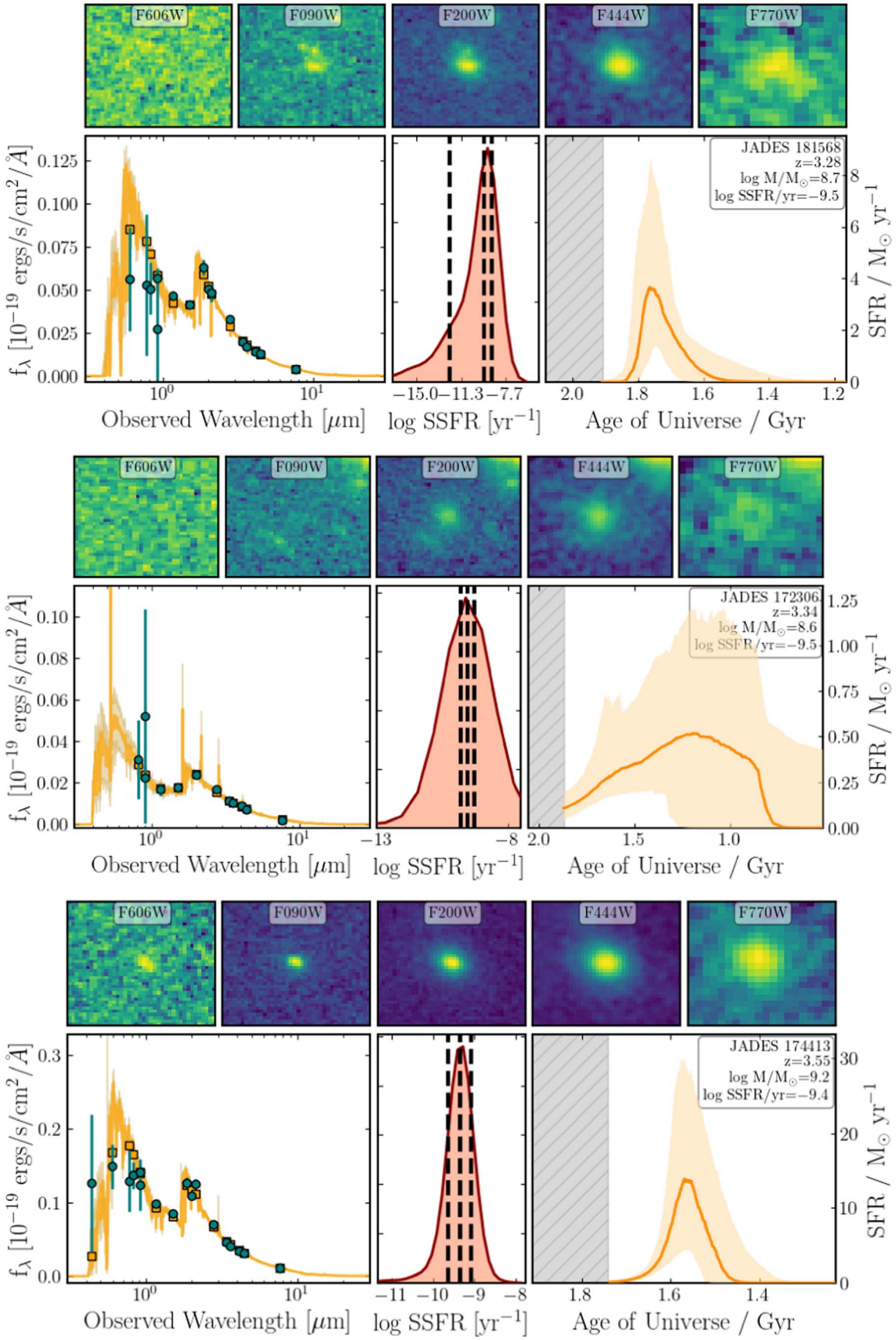

Figure A2. Properties of the tentative poststarburst galaxies selected via B19. Top rows for each source: F606W, F090W, F200W, F444W, F770W cutouts, 1.″2 on a side. Bottom rows for each source: the SEDs (left), SSFR posterior distributions (middle), and SFHs (right).

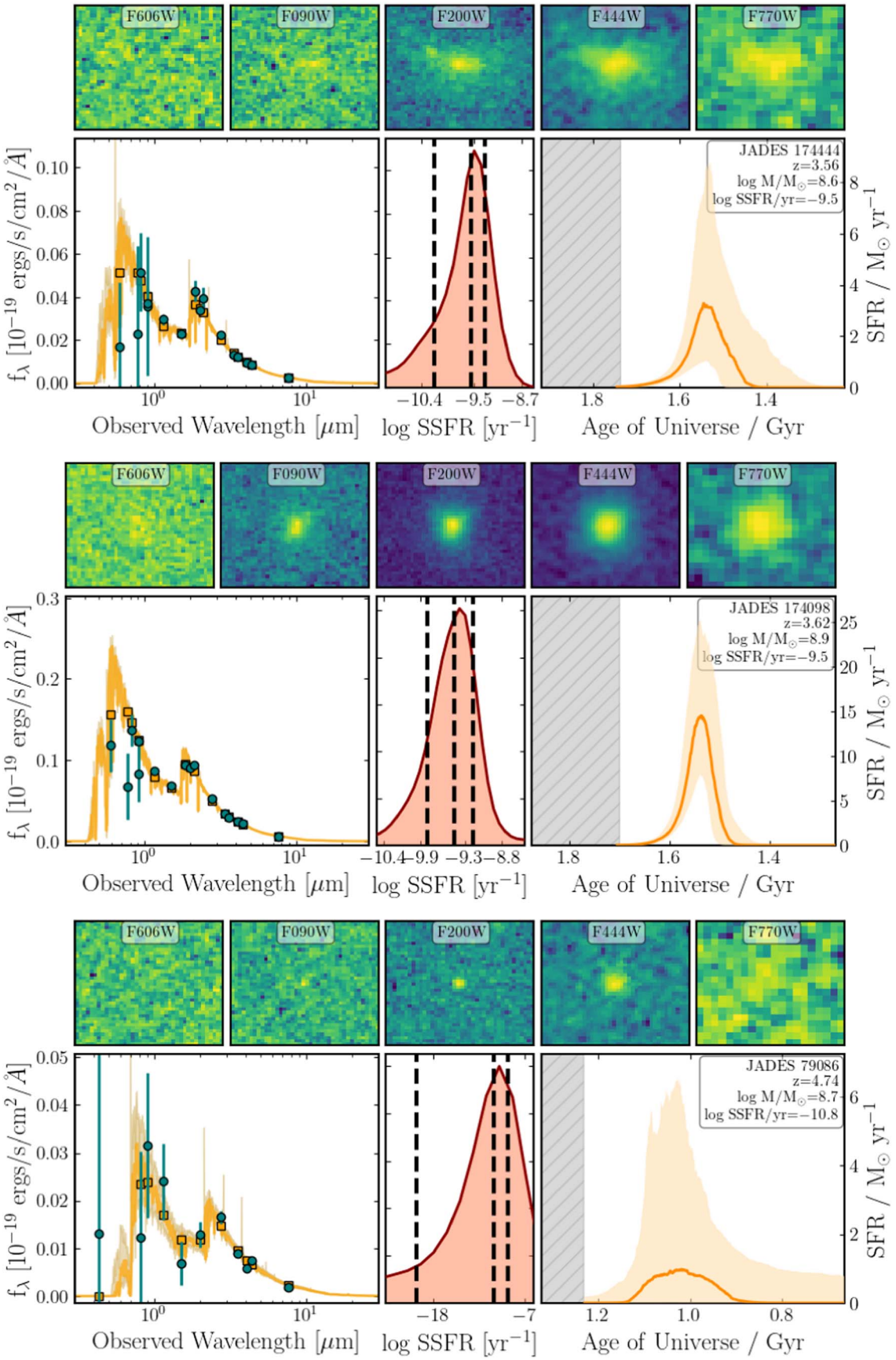

Figure A2. (Continued.)

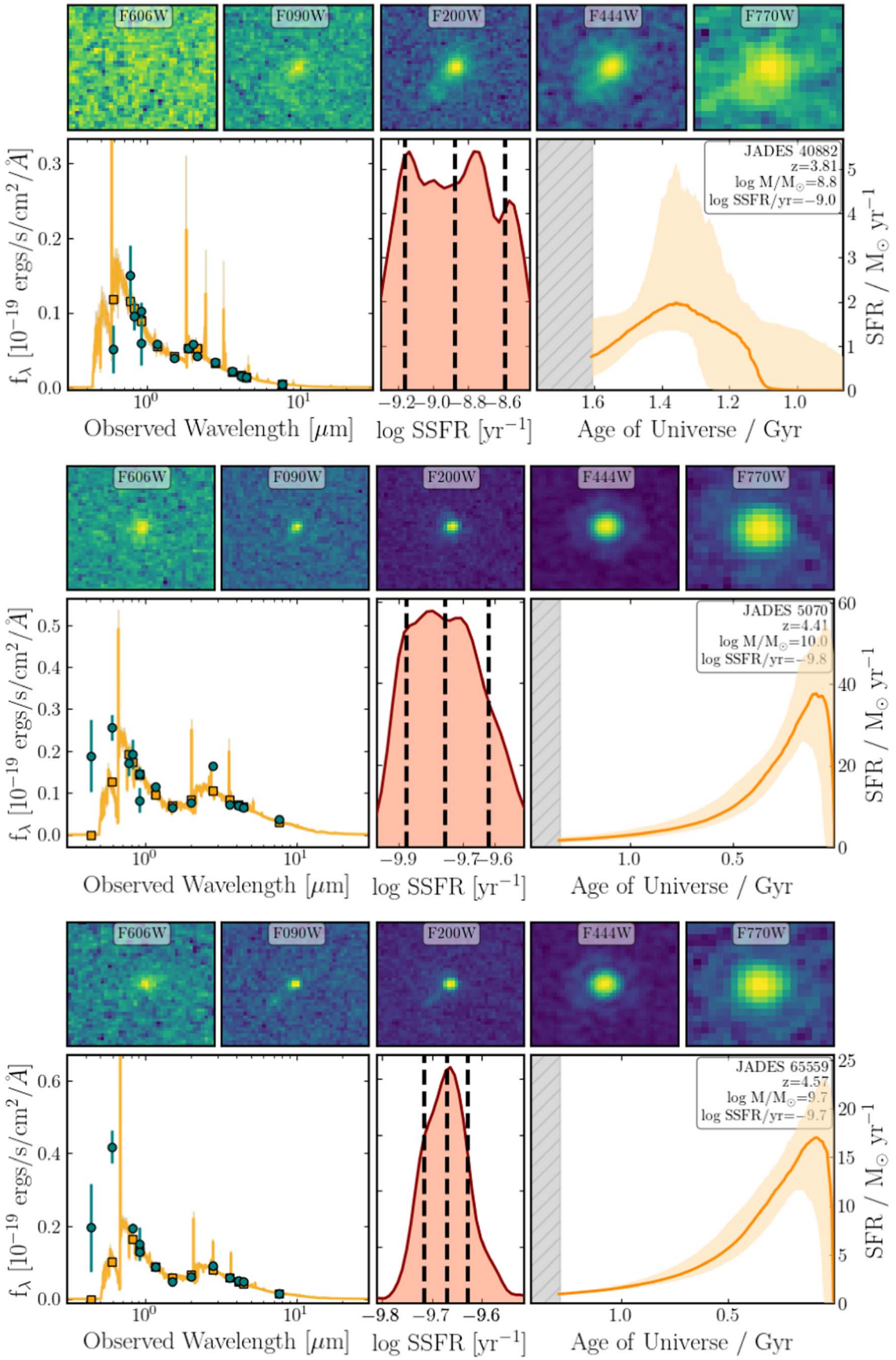

Figure A2. (Continued.)

Appendix B
Overdensities at $z = 3$–4 in JADES GOODS-S

In this section, we outline the identification of the galaxy overdensities discussed in Section 5.3. For an overdensity associated with the Cosmic Rose (Figure 8), we searched the v0.8.1 JADES GOODS-S photometric catalog (Rieke et al. 2023) for relatively bright (<28 mag in F200W, F277W, F356W, and F444W) galaxies at $3.55 < z_{\rm phot} < 3.85$ using PSF-matched Kron photometry and EAZY photometric redshifts (Hainline et al. 2024). We choose to not make any cut on the photometric redshift uncertainty since this would bias against the QG and/or PSB galaxy candidates identified here. Following these selections, we are left with a photometric sample of $N = 940$ sources.

Following the methodology briefly described in Sandles et al. (2023), we then utilize a kernel density estimator (KDE) assuming Gaussian kernels to estimate the underlying density field of our photometric sample. The assumed bandwidth (or smoothing scale) is optimized by maximizing the likelihood cross-validation quantity (Chartab et al. 2020), which provides an optimal trade-off between undersmoothing and oversmoothing. Our optimized bandwidth is 0.86 cMpc, which roughly corresponds to 0.′42 at $z = 3.7$. We note that KDEs are effective in estimating the underlying density field at locations that are far from the edges of the footprint; however, they tend to underestimate densities near edges. To counter this, we implement a correction factor as described in Taamoli et al. (2024). The KDE method identifies $N = 4$ spatially distinct galaxy overdensities, which have peak significance levels larger than 4σ, where σ corresponds to the standard deviation of the density values across the entire JADES GOODS-S field. One of these identified galaxy overdensities spatially and kinematically encompasses the Cosmic Rose, containing $N = 16$ potential members with a peak significance level of roughly 4.3σ at $\langle z_{\rm phot} \rangle = 3.759$. The maximum separation between these potential constituent members is 0.79 cMpc, or roughly 0.′37. The full $z \sim 3.7$ overdensity identified here is coincident with a structure ("Sparsh" at $\langle z \rangle = 3.696$) independently identified using spectroscopic and photometric optical catalogs and Voronoi tessellation Monte Carlo mapping in Shah et al. (2023).

We repeat this procedure at $3.25 < z < 3.55$, finding $N_{\rm gal} = 814$ galaxies. We estimate the underlying density field using an optimized bandwidth is 0.9 cMpc and find a $>4\sigma$ peak at $z \sim 3.4$ (Figure B1). This overdensity is coincident with "Smruti" at $\langle z \rangle = 3.466$ identified in Shah et al. (2023).

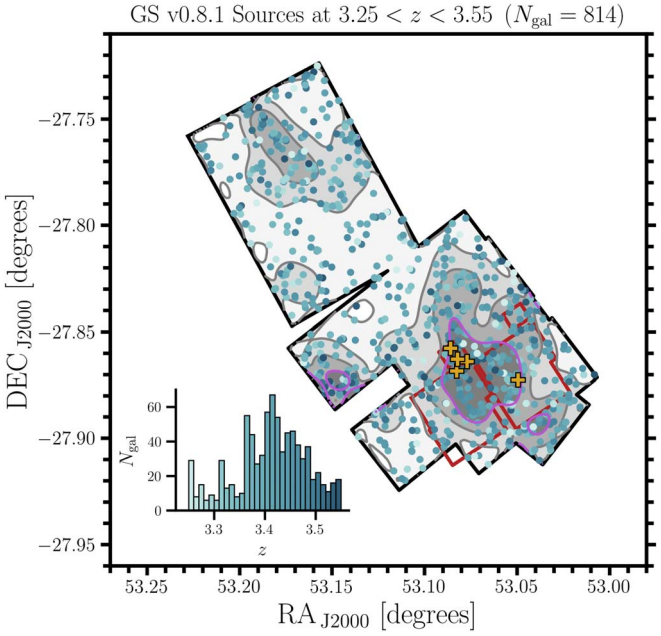

Figure B1. Overdensities of galaxies at $3.25 < z < 3.55$ in the JADES NIRCam (black outline) and MIRI parallel (red outline) field of views. Contours increment by 1σ, with the purple contour outlining 4σ peaks. The yellow pluses show low-mass PSBs that are part of the $z \sim 3.4$ overdensity.

ORCID iDs

Stacey Alberts https://orcid.org/0000-0002-8909-8782
Christina C. Williams https://orcid.org/0000-0003-2919-7495
Jakob M. Helton https://orcid.org/0000-0003-4337-6211
Katherine A. Suess https://orcid.org/0000-0002-1714-1905
Zhiyuan Ji https://orcid.org/0000-0001-7673-2257
Irene Shivaei https://orcid.org/0000-0003-4702-7561
Jianwei Lyu https://orcid.org/0000-0002-6221-1829
George Rieke https://orcid.org/0000-0003-2303-6519
William M. Baker https://orcid.org/0000-0003-0215-1104
Nina Bonaventura https://orcid.org/0000-0001-8470-7094
Andrew J. Bunker https://orcid.org/0000-0002-8651-9879
Stefano Carniani https://orcid.org/0000-0002-6719-380X
Stephane Charlot https://orcid.org/0000-0003-3458-2275
Emma Curtis-Lake https://orcid.org/0000-0002-9551-0534
Francesco D'Eugenio https://orcid.org/0000-0003-2388-8172
Daniel J. Eisenstein https://orcid.org/0000-0002-2929-3121
Anna de Graaff https://orcid.org/0000-0002-2380-9801
Kevin N. Hainline https://orcid.org/0000-0003-4565-8239
Ryan Hausen https://orcid.org/0000-0002-8543-761X
Benjamin D. Johnson https://orcid.org/0000-0002-9280-7594
Roberto Maiolino https://orcid.org/0000-0002-4985-3819
Eleonora Parlanti https://orcid.org/0000-0002-7392-7814
Marcia J. Rieke https://orcid.org/0000-0002-7893-6170
Brant E. Robertson https://orcid.org/0000-0002-4271-0364
Yang Sun https://orcid.org/0000-0001-6561-9443
Sandro Tacchella https://orcid.org/0000-0002-8224-4505
Christopher N. A. Willmer https://orcid.org/0000-0001-9262-9997
Chris J. Willott https://orcid.org/0000-0002-4201-7367

References

Akhshik, M., Whitaker, K. E., Leja, J., et al. 2021, ApJL, 907, L8
Akhshik, M., Whitaker, K. E., Leja, J., et al. 2023, ApJ, 943, 179
Alatalo, K., Lisenfeld, U., Lanz, L., et al. 2016, ApJ, 827, 106
Alberts, S., Lyu, J., Shivaei, I., et al. 2024, arXiv:2405.15972
Alberts, S., & Noble, A. 2022, Univ, 8, 554
Antwi-Danso, J., Papovich, C., Esdaile, J., et al. 2023a, arXiv:2307.09590
Antwi-Danso, J., Papovich, C., Leja, J., et al. 2023b, ApJ, 943, 166
Arrabal Haro, P., Dickinson, M., Finkelstein, S. L., et al. 2023, Natur, 622, 707
Astropy Collaboration, Price-Whelan, A. M., Lim, P. L., et al. 2022, ApJ, 935, 167
Astropy Collaboration, Price-Whelan, A. M., Sipőcz, B. M., et al. 2018, AJ, 156, 123
Astropy Collaboration, Robitaille, T. P., Tollerud, E. J., et al. 2013, A&A, 558, A33
Bahé, Y. M., Schaye, J., Barnes, D. J., et al. 2019, MNRAS, 485, 2287
Baker, W. M., Maiolino, R., Bluck, A. F. L., et al. 2024, MNRAS, 534, 30
Baker, W. M., Tacchella, S., Johnson, B. D., et al. 2023b, arXiv:2306.02472
Baldry, I. K., Glazebrook, K., Brinkmann, J., et al. 2004, ApJ, 600, 681
Balogh, M. L., Navarro, J. ., & Morris, S. L. 2000, ApJ, 540, 113

Beckwith, S. V. W., Stiavelli, M., Koekemoer, A. M., et al. 2006, AJ, 132, 1729
Belli, S., Contursi, A., Genzel, R., et al. 2021, ApJL, 909, L11
Belli, S., Genzel, R., Förster Schreiber, N. M., et al. 2017, ApJL, 841, L6
Belli, S., Newman, A. B., & Ellis, R. S. 2019, ApJ, 874, 17
Benítez-Llambay, A., Navarro, J. . F., Abadi, M. G., et al. 2013, ApJL, 763, L41
Bezanson, R., Spilker, J., Williams, C. C., et al. 2019, ApJL, 873, L19
Birkin, J. E., Weiss, A., Wardlow, J. L., et al. 2021, MNRAS, 501, 3926
Blánquez-Sesé, D., Magdis, G. E., Gómez-Guijarro, C., et al. 2023, A&A, 679, L2
Bluck, A. F. L., Conselice, C. J., Ormerod, K., et al. 2024, ApJ, 961, 163
Bluck, A. F. L., Maiolino, R., Brownson, S., et al. 2022, A&A, 659, A160
Bluck, A. F. L., Maiolino, R., Piotrowska, J. M., et al. 2020, MNRAS, 499, 230
Bluck, A. F. L., Mendel, J. T., Ellison, S. L., et al. 2014, MNRAS, 441, 599
Bluck, A. F. L., Mendel, J. T., Ellison, S. L., et al. 2016, MNRAS, 462, 2559
Bluck, A. F. L., Piotrowska, J. ., & Maiolino, R. 2023, ApJ, 944, 108
Boselli, A., Fossati, M., & Sun, M. 2022, A&ARv, 30, 3
Brammer, G. B., van Dokkum, P. G., & Coppi, P. 2008, ApJ, 686, 1503
Bruzual, G., & Charlot, S. 2003, MNRAS, 344, 1000
Buchner, J., Georgakakis, A., Nandra, K., et al. 2014, A&A, 564, A125
Bullock, J. S., & Boylan-Kolchin, M. 2017, ARA&A, 55, 343
Butcher, H., & Oemler, A., Jr 1978, ApJ, 226, 559
Byler, N., Dalcanton, J. ., Conroy, C., & Johnson, B. D. 2017, ApJ, 840, 44
Caliendo, J. . N., Whitaker, K. E., Akhshik, M., et al. 2021, ApJL, 910, L7
Calzetti, D., Armus, L., Bohlin, R. C., et al. 2000, ApJ, 533, 682
Carnall, A. C., Leja, J., Johnson, B. D., et al. 2019a, ApJ, 873, 44
Carnall, A. C., McLeod, D. J., McLure, R. J., et al. 2023a, MNRAS, 520, 3974
Carnall, A. C., McLure, R. J., Dunlop, J. S., & Davé, R. 2018, MNRAS, 480, 4379
Carnall, A. C., McLure, R. J., Dunlop, J. S., et al. 2019b, MNRAS, 490, 417
Carnall, A. C., McLure, R. J., Dunlop, J. S., et al. 2023b, Natur, 619, 716
Carnall, A. C., Walker, S., McLure, R. J., et al. 2020, MNRAS, 496, 695
Casey, C. M., Kartaltepe, J. S., Drakos, N. E., et al. 2023, ApJ, 954, 31
Castignani, G., Combes, F., Jablonka, P., et al. 2022, A&A, 657, A9
Cecchi, R., Bolzonella, M., Cimatti, A., & Girelli, G. 2019, ApJL, 880, L14
Chartab, N., Mobasher, B., Darvish, B., et al. 2020, ApJ, 890, 7
Chevallard, J., & Charlot, S. 2016, MNRAS, 462, 1415
Cochrane, R. K., Hayward, C. C., & Anglés-Alcázar, D. 2022, ApJL, 939, L27
Cortese, L., Catinella, B., & Smith, R. 2021, PASA, 38, 35
Crain, R. A., Schaye, J., Bower, R. G., et al. 2015, MNRAS, 450, 1937
Cullen, F., McLure, R. J., Dunlop, J. S., et al. 2019, MNRAS, 487, 2038
Cutler, S. E., Whitaker, K. E., Weaver, J. R., et al. 2024, ApJL, 967, L23
Davé, R., Finlator, K., & Oppenheimer, B. D. 2012, MNRAS, 421, 98
Davidzon, I., Ilbert, O., Laigle, C., et al. 2017, A&A, 605, A70
Davis, F., Kaviraj, S., Hardcastle, M. J., et al. 2022, MNRAS, 511, 4109
de Graaff, A., Setton, D. J., Brammer, G., et al. 2024, arXiv:2404.05683
Desprez, G., Martis, N. S., Asada, Y., et al. 2024, MNRAS, 530, 2935
D'Eugenio, C., Daddi, E., Gobat, R., et al. 2020, ApJL, 892, L2
D'Eugenio, F., Perez-Gonzalez, P., Maiolino, R., et al. 2024, NatAs
Díaz-García, L. A., Cenarro, A. J., López-Sanjuan, C., et al. 2019, A&A, 631, A156
Dome, T., Tacchella, S., Fialkov, A., et al. 2024, MNRAS, 527, 2139
Efstathiou, G. 1992, MNRAS, 256, 43P
Eisenstein, D. J., Willott, C., Alberts, S., et al. 2023, arXiv:2306.02465
Endsley, R., Stark, D. P., Whitler, L., et al. 2023, MNRAS, 524, 2312
Esdaile, J., Labbé, I., Glazebrook, K., et al. 2021, AJ, 162, 225
Fang, J. J., Faber, S. M., Koo, D. C., et al. 2018, ApJ, 858, 100
Ferland, G. J., Porter, R. L., van Hoof, P. A. M., et al. 2013, RMxAA, 49, 137
Feroz, F., Hobson, M. P., Cameron, E., & Pettitt, A. N. 2019, OJAp, 2, 10
Fitzpatrick, E. L., Ribas, I., Guinan, E. F., et al. 2002, ApJ, 564, 260
Fontana, A., Santini, P., Grazian, A., et al. 2009, A&A, 501, 15
Forrest, B., Marsan, Z. C., Annunziatella, M., et al. 2020, ApJ, 903, 47
French, K. D., Yang, Y., Zabludoff, A., et al. 2015, ApJ, 801, 1
Gaia Collaboration, Brown, A. G. A., Vallenari, A., et al. 2018, A&A, 616, A1
Gallazzi, A., Bell, E. F., Zibetti, S., Brinchmann, J., & Kelson, D. D. 2014, ApJ, 788, 72
Gáspár, A., Rieke, G. H., Guillard, P., et al. 2021, PASP, 133, 014504
Geha, M., Blanton, M. R., Yan, R., & Tinker, J. L. 2012, ApJ, 757, 85
Gelli, V., Salvadori, S., Ferrara, A., & Pallottini, A. 2024, ApJ, 964, 76
Giménez-Arteaga, C., Oesch, P. A., Brammer, G. B., et al. 2023, ApJ, 948, 126
Girelli, G., Bolzonella, M., & Cimatti, A. 2019, A&A, 632, A80
Glazebrook, K., Nanayakkara, T., Jacobs, C., et al. 2023, ApJL, 947, L25
Glazebrook, K., Schreiber, C., Labbé, I., et al. 2017, Natur, 544, 71
Gobat, R., Daddi, E., Magdis, G., et al. 2018, NatAs, 2, 239
Gould, K. M. L., Brammer, G., Valentino, F., et al. 2023, AJ, 165, 248
Hainline, K. N., Johnson, B. D., Robertson, B., et al. 2024, ApJ, 964, 71
Hamadouche, M. L., Carnall, A. C., McLure, R. J., et al. 2022, MNRAS, 512, 1262
Hamadouche, M. L., Carnall, A. C., McLure, R. J., et al. 2023, MNRAS, 521, 5400
Harikane, Y., Zhang, Y., Nakajima, K., et al. 2023, ApJ, 959, 39
Hubble, E. P. 1926, ApJ, 64, 321
Illingworth, G., Magee, D., Bouwens, R., et al. 2016, arXiv:1606.00841
Ji, Z., Giavalisco, M., Williams, C. C., et al. 2018, ApJ, 862, 135
Johnson, B. D., Leja, J., Conroy, C., & Speagle, J. S. 2021, ApJS, 254, 22
Kauffmann, G., Heckman, T. M., White, S. D. M., et al. 2003, MNRAS, 341, 33
Kaushal, Y., Nersesian, A., Bezanson, R., et al. 2024, ApJ, 961, 118
Kaviraj, S., Martin, G., & Silk, J. 2019, MNRAS, 489, L12
Kawinwanichakij, L., Quadri, R. F., Papovich, C., et al. 2016, ApJ, 817, 9
Kokorev, V., Jin, S., Magdis, G. E., et al. 2023, ApJL, 945, L25
Koudmani, S., Henden, N. A., & Sijacki, D. 2021, MNRAS, 503, 3568
Kriek, M., Beverage, A. G., Price, S. H., et al. 2024, ApJ, 966, 36
Kriek, M., Conroy, C., van Dokkum, P. G., et al. 2016, Natur, 540, 248
Kroupa, P. 2001, MNRAS, 322, 231
Kubo, M., Nagao, T., Uchiyama, H., et al. 2024, MNRAS, 527, 403
Labbé, I., Huang, J., Franx, M., et al. 2005, ApJL, 624, L81
Labbé, I., van Dokkum, P., Nelson, E., et al. 2023, Natur, 616, 266
Larson, R. B., Tinsley, B. M., & Caldwell, C. N. 1980, ApJ, 237, 692
Lee, M. M., Steidel, C. C., Brammer, G., et al. 2024, MNRAS, 527, 9529
Leja, J., Carnall, A. C., Johnson, B. D., Conroy, C., & Speagle, J. S. 2019a, ApJ, 876, 3
Leja, J., Tacchella, S., & Conroy, C. 2019b, ApJL, 880, L9
Leung, H.-H., Wild, V., Papathomas, M., et al. 2024, MNRAS, 528, 4029
Lilly, S. J., Carollo, C. M., Pipino, A., Renzini, A., & Peng, Y. 2013, ApJ, 772, 119
Long, A. S., Antwi-Danso, J., Lambrides, E. L., et al. 2024, ApJ, 970, 68
Looser, T. J., D'Eugenio, F., Maiolino, R., et al. 2024, Natur, 629, 53
Lovell, C. C., Roper, W., Vijayan, A. P., et al. 2023, MNRAS, 525, 5520
Lovell, C. C., Vijayan, A. P., Thomas, P. A., et al. 2021, MNRAS, 500, 2127
Lyu, J., Alberts, S., Rieke, G. H., & Rujopakarn, W. 2022, ApJ, 941, 191
Magdis, G. E., Gobat, R., Valentino, F., et al. 2021, A&A, 647, A33
Maiolino, R., & Mannucci, F. 2019, A&ARv, 27, 3
Maiolino, R., Scholtz, J., Curtis-Lake, E., et al. 2023, arXiv:2308.01230
Man, A., & Belli, S. 2018, NatAs, 2, 695
Marchesini, D., Brammer, G., Morishita, T., et al. 2023, ApJL, 942, L25
Marchesini, D., Whitaker, K. E., Brammer, G., et al. 2010, ApJ, 725, 1277
Marsan, Z. C., Muzzin, A., Marchesini, D., et al. 2022, ApJ, 924, 25
McQuinn, Kristen, B. W., van Zee, L., & Skillman, E. D. 2019, ApJ, 886, 74
Merlin, E., Fontana, A., Castellano, M., et al. 2018, MNRAS, 473, 2098
Merlin, E., Fortuni, F., Torelli, M., et al. 2019, MNRAS, 490, 3309
Morishita, T., Abdurro'uf, Hirashita, H., et al. 2022, ApJ, 938, 144
Muzzin, A., Marchesini, D., Stefanon, M., et al. 2013, ApJ, 777, 18
Nanayakkara, T., Glazebrook, K., Jacobs, C., et al. 2024, NatSR, 14, 3724
Nersesian, A., van der Wel, A., Gallazzi, A., et al. 2024, A&A, 681, A94
Newman, A. B., Belli, S., Ellis, R. S., & Patel, S. G. 2018, ApJ, 862, 125
Noll, S., Burgarella, D., Giovannoli, E., et al. 2009, A&A, 507, 1793
Oesch, P. A., Brammer, G., Naidu, R. P., et al. 2023, MNRAS, 525, 2864
Oke, J. B., & Gunn, J. E. 1983, ApJ, 266, 713
Ormerod, K., Conselice, C. J., Adams, N. J., et al. 2023, MNRAS, 527, 6110
Pacifici, C., Kassin, S. A., Weiner, B. J., et al. 2016, ApJ, 832, 79
Papovich, C., Cole, J. W., Yang, G., et al. 2023, ApJL, 949, L18
Park, M., Belli, S., Conroy, C., et al. 2023, ApJ, 953, 119
Peng, Y., Maiolino, R., & Cochrane, R. 2015, Natur, 521, 192
Peng, Y.-j., Lilly, S. J., Kovač, K., et al. 2010, ApJ, 721, 193
Peng, Y.-j., Lilly, S. J., Renzini, A., & Carollo, M. 2012, ApJ, 757, 4
Pérez-González, P. G., Barro, G., Annunziatella, M., et al. 2023, ApJL, 946, L16
Piotrowska, J. M., Bluck, A. F. L., Maiolino, R., & Peng, Y. 2022, MNRAS, 512, 1052
Popesso, P., Concas, A., Cresci, G., et al. 2023, MNRAS, 519, 1526
Rieke, M., Robertson, B., Tacchella, S., et al. 2023, ApJS, 269, 16
Rowlands, K., Wild, V., Bourne, N., et al. 2018, MNRAS, 473, 1168
Rowlands, K., Wild, V., Nesvadba, N., et al. 2015, MNRAS, 448, 258
Salim, S., Boquien, M., & Lee, J. C. 2018, ApJ, 859, 11
Sanders, R. L., Shapley, A. E., Jones, T., et al. 2021, ApJ, 914, 19
Sandles, L., D'Eugenio, F., Helton, J. M., et al. 2023, arXiv:2307.08633
Schaye, J., Crain, R. A., Bower, R. G., et al. 2015, MNRAS, 446, 521
Schreiber, C., Glazebrook, K., Nanayakkara, T., et al. 2018a, A&A, 618, A85
Schreiber, C., Labbé, I., Glazebrook, K., et al. 2018b, A&A, 611, A22

Setton, D. J., Khullar, G., Miller, T. B., et al. 2024, ApJ, 974, 145
Shah, E. A., Lemaux, B., Forrest, B., et al. 2024, MNRAS, 529, 873
Shahidi, A., Mobasher, B., Nayyeri, H., et al. 2020, ApJ, 897, 44
Shibuya, T., Ouchi, M., & Harikane, Y. 2015, ApJS, 219, 15
Silk, J. 2017, ApJL, 839, L13
Somerville, R. S., & Davé, R. 2015, ARA&A, 53, 51
Spilker, J. S., Suess, K. A., Setton, D. J., et al. 2022, ApJL, 936, L11
Spitler, L. R., Straatman, C. M. S., Labbé, I., et al. 2014, ApJL, 787, L36
Stanway, E. R., McMahon, R. G., & Bunker, A. J. 2005, MNRAS, 359, 1184
Straatman, C. M. S., Labbé, I., Spitler, L. R., et al. 2014, ApJL, 783, L14
Straatman, C. M. S., Labbé, I., Spitler, L. R., et al. 2015, ApJL, 808, L29
Straatman, C. M. S., Spitler, L. R., Quadri, R. F., et al. 2016, ApJ, 830, 51
Strait, V., Brammer, G., Muzzin, A., et al. 2023, ApJL, 949, L23
Suess, K. A., Bezanson, R., Spilker, J. S., et al. 2017, ApJL, 846, L14
Suess, K. A., Kriek, M., Bezanson, R., et al. 2022a, ApJ, 926, 89
Suess, K. A., Leja, J., Johnson, B. D., et al. 2022b, ApJ, 935, 146
Suzuki, T. L., Glazebrook, K., Schreiber, C., et al. 2022, ApJ, 936, 61
Taamoli, S., Mobasher, B., Chartab, N., et al. 2024, ApJ, 966, 18
Tacchella, S., Bose, S., Conroy, C., Eisenstein, D. J., & Johnson, B. D. 2018, ApJ, 868, 92
Tacchella, S., Conroy, C., Faber, S. M., et al. 2022a, ApJ, 926, 134
Tacchella, S., Finkelstein, S. L., Bagley, M., et al. 2022b, ApJ, 927, 170
Tacchella, S., Johnson, B. D., Robertson, B. E., et al. 2023, MNRAS, 522, 6236
Tomczak, A. R., Quadri, R. F., Tran, K.-V. H., et al. 2014, ApJ, 783, 85
Trebitsch, M., Volonteri, M., Dubois, Y., & Madau, P. 2018, MNRAS, 478, 5607
Trussler, J., Maiolino, R., Maraston, C., et al. 2020, MNRAS, 491, 5406
Valentino, F., Brammer, G., Gould, K. M. L., et al. 2023, ApJ, 947, 20
Valentino, F., Tanaka, M., Davidzon, I., et al. 2020, ApJ, 889, 93
Vijayan, A. P., Lovell, C. C., Wilkins, S. M., et al. 2021, MNRAS, 501, 3289
Vijayaraghavan, R., & Ricker, P. M. 2013, MNRAS, 435, 2713
Vulcani, B., Poggianti, B. M., Moretti, A., et al. 2021, ApJ, 914, 27
Weaver, J. R., Kauffmann, O. B., Ilbert, O., et al. 2022, ApJS, 258, 11
Whitaker, K. E., Ashas, M., Illingworth, G., et al. 2019, ApJS, 244, 16
Whitaker, K. E., Kriek, M., van Dokkum, P. G., et al. 2012, ApJ, 745, 179
Whitaker, K. E., Labbé, I., van Dokkum, P. G., et al. 2011, ApJ, 735, 86
Whitaker, K. E., Narayanan, D., Williams, C. C., et al. 2021a, ApJL, 922, L30
Whitaker, K. E., van Dokkum, P. G., Brammer, G., et al. 2010, ApJ, 719, 1715
Whitaker, K. E., Williams, C. C., Mowla, L., et al. 2021b, Natur, 597, 485
Wild, V., Almaini, O., Dunlop, J., et al. 2016, MNRAS, 463, 832
Wilkins, S. M., Bunker, A. J., Stanway, E., Lorenzoni, S., & Caruana, J. 2011, MNRAS, 417, 717
Williams, C. C., Alberts, S., Ji, Z., et al. 2024, ApJ, 968, 34
Williams, C. C., Spilker, J. S., Whitaker, K. E., et al. 2021, ApJ, 908, 54
Williams, R. J., Quadri, R. F., Franx, M., van Dokkum, P., & Labbé, I. 2009, ApJ, 691, 1879
Woodrum, C., Williams, C. C., Rieke, M., et al. 2022, ApJ, 940, 39
Wright, G. S., Rieke, G. H., Glasse, A., et al. 2023, PASP, 135, 048003
Xiao, M., Oesch, P., Elbaz, D., et al. 2023, arXiv:2309.02492
Yang, G., Papovich, C., Bagley, M., et al. 2023, ApJ, 956, 12